1 Revised manuscript

2 Shearing within lower crust during progressive retrogression: structural

3 analysis of gabbroic rocks from the Godzilla Mullion, an oceanic core

4 complex in the Parece Vela backarc basin

5

6 Yumiko Harigane[a*], Katsuyoshi Michibayashi[b], Yasuhiko Ohara[c, d]

7 [a]*Educational Division of Science and Technology, Shizuoka University, Shizuoka 422-8529, Japan*

8 [b]*Institute of Geosciences, Shizuoka University, Shizuoka 422-8529, Japan*

9 [c]*Hydrographic and Oceanographic Department of Japan, Tokyo 104-0045, Japan*

10 [d]*Institute for Research on Earth Evolution, Japan Agency for Marine-Earth Science and Technology,*

11 *Kanagawa 236-0016, Japan*

12

13 *Corresponding author. Tel: +81-54-238-4788; Fax: +81-54-238-0491;

14 E-mail address: f5644006@ipc.shizuoka.ac.jp (Y. Harigane)

15

16 **Abstract**

17   Microstructural and petrological analyses of gabbroic rocks sampled from the
18 Godzilla Mullion, located along the Parece Vela Basin spreading ridge (Parece Vela
19 Rift), Philippine Sea, reveal the development of a ductile shear zone in the lower crust.
20 The shear zone is interpreted to represent a detachment fault within an oceanic core
21 complex. Microstructures indicative of intense deformation, characterized by
22 porphyroclastic textures consisting dominantly of coarse plagioclase porphyroclasts and
23 lesser clinopyroxene porphyroclasts in a fine-grained matrix, are observed within
24 samples of gabbroic rocks dredged near the breakaway area of the Godzilla Mullion
25 (dredge site D6). Samples are classified into three types based upon the grain size of
26 fine-grained plagioclase in the matrix: coarse (80–130μm), medium (25μm), and fine
27 (~10μm). Although the chemical composition of plagioclase porphyroclasts is
28 consistently An 40–50 among all sample types, the compositions of fine grains in the
29 matrix vary with decreasing grain size, being An 40–50 for the coarse-type, An 30–40
30 for the medium-type, and An 5–30 for the fine-type. This finding implies that the
31 composition of fine-grained plagioclase in the matrix is related to the following
32 retrograde reaction that occurred during deformation: clinopyroxene + plagioclase +

33 Fe-Ti oxide + fluid → hornblende + plagioclase. Plagioclase crystal-preferred

34 orientations also show a gradual change with grain size, varying from a (010)[100]
35 pattern for the coarse-type, (010)[100] and (001)[100] patterns for the medium-type,
36 and a weak (001)[100] pattern or random orientations for the fine-type. These patterns
37 are interpreted to result from a change in the deformation mechanism of plagioclase
38 from dislocation creep to grain-size-sensitive creep with decreasing temperature,
39 thereby leading to strain softening and localization during cooling. Although secondary
40 amphibole occurs ubiquitously within all samples, the chemical composition of
41 amphibole varies from pargasitic hornblende (i.e. brown hornblende) to actinolite (i.e.
42 green hornblende) within each of the sample types. However, amphibole in the
43 coarse-type shows no evidence of deformation, whereas brown hornblende in the
44 medium- and fine-types is plastically deformed. As a consequence, we argue that the
45 microstructural development of the gabbroic rocks occurred during uplift-related
46 cooling of the gabbro body and that a primary shear zone developed near the breakaway
47 area at depth under anhydrous conditions at high temperatures above 850 °C; the shear
48 zone subsequently evolved during progressive retrogression in association with
49 hydration of the shear zone, possibly resulting in the development of the detachment
50 fault that gave rise to the Godzilla Mullion.

51

52 *Key words*: Godzilla Mullion, Detachment fault, Oceanic Core Complex, Philippine Sea,
53 Gabbro, Shear zone

1. Introduction

Oceanic core complexes (OCCs) are bathymetric features that were first identified along the Mid-Atlantic Ridge (e.g., Karson, 1990; Tucholke and Lin, 1994; Cann et al., 1997; Blackman et al., 1998; Tucholke et al., 1998). Based on morphological characteristics, OCCs usually occur close to the intersection of transform faults and the axis of a spreading ridge (i.e., a ridge-transform intersection), and are characterized by a domal surface, corrugations oriented parallel to the spreading direction, a high mantle Bouguer anomaly, and exposed lower crust and mantle material (e.g., Blackman et al., 1998; Tucholke et al., 1998). By analogy to continental metamorphic core complexes, it has been suggested that OCCs along a spreading axis represent the exhumed footwalls of oceanic detachment faults (e.g., Karson, 1990; Cann et al., 1997; Blackman et al., 1998; Tucholke et al., 1998; Karson, 1999; Dick et al., 1991, 2000; MacLeod et al., 2002; Escartin et al., 2003; Ildefonse et al., 2007; Smith et al., 2008).

Ohara et al. (2001) reported an extremely large OCC in the Parece Vela backarc basin within the Philippine Sea (Fig. 1). As this structure is approximately 10 times larger than those commonly found along the Mid-Atlantic Ridge, Ohara et al. (2003a) termed this complex the Godzilla Mullion. Although OCCs generally develop at ultraslow- (full rate: ~1.2-2 cm/y; Dick et al., 2003) or slow-spreading ridges (full rate: 1-4 cm/y) such as the Southwest Indian Ridge and the Mid-Atlantic Ridge, the Godzilla Mullion developed at a spreading ridge that records intermediate spreading rates (full rate: 7.0 cm/y; Ohara et al., 2001), similar to those of the Chile Ridge (e.g., Martinez et al., 1998), the Australian-Antarctic Discordance (e.g., Christie et al., 1998; Okino et al., 2004), and the 25°S OCC upon the Central Indian Ridge (e.g., Kumagai et al., 2006). The Godzilla Mullion is also unique in that it extends along the full length of the spreading segment (Ohara et al., 2001).

Fault rocks derived from lithospheric mantle and lower oceanic crust occur on the surface of the Godzilla Mullion, indicating the occurrence of a detachment fault at the seafloor surface: the mechanism of the development of these fault rocks remains unknown. In this study, we investigate deformed gabbroic rocks dredged from the surface of the Godzilla Mullion (Ohara et al., 2003a). We describe a systematic temporal change in both deformation microstructures and the chemical composition of plagioclase and amphibole in gabbroic rocks, possibly associated with the development of a detachment fault within the Godzilla Mullion at depth.

2. Geological setting
2.1. Parece Vela Basin

The Philippine Sea contains a number of active and inactive arcs and backarc basins. The Parece Vela Basin is an extinct backarc basin located between two remnant arcs: the Kyushu-Palau Ridge and the West Mariana Ridge (Fig. 1). The center of the Parece Vela Basin is characterized by a N–S-trending chain of diamond-shaped

depressions termed the Parece Vela Rift (Kasuga and Ohara, 1997). The spreading history of the Parece Vela Basin involved two stages: an E–W rifting/spreading event from 26 to 19–20 Ma, followed by NE–SW spreading until 12 Ma (Okino et al., 1998, 1999; Ohara et al., 2001). The ridge axis (the Parece Vela Rift) became highly segmented during the second stage of the spreading history, resulting in the development of prominent fracture zones (Ohara et al., 2001). Magnetic anomaly data indicate a spreading rate of 8.8 cm/y (full rate) in the western Parece Vela Basin during the first stage of spreading (Okino et al., 1998) and a rate of 7.0 cm/y (full rate) during the second stage (Ohara et al., 2001).

2.2. Bathymetry of the Godzilla Mullion

Bathymetry and gravity-anomaly data for the Godzilla Mullion have been reported by Ohara et al. (2001). The Godzilla Mullion is located on the southwest flank of the inactive S1 spreading segment. Topographic corrugations oriented perpendicular to the Parece Vela Rift are clearly visible across the surface of the Godzilla Mullion (Fig. 1). These corrugations extend 55 km along the axis and 125 km perpendicular to the axis (Fig. 1), defining an area that is more than 10 times larger than the OCCs described at the Mid-Atlantic Ridge (Ohara et al., 2001). Further away from the spreading axis, distinct low-relief, linear abyssal hills are oriented parallel to the strike of the axis (Fig. 1).

3. Dredge samples from the breakaway area

Dredge site D6 is located at the southwestern, distal end of the Godzilla Mullion (Fig. 1), ~15 km from the breakaway area where the fault initially nucleated (Tucholke et al., 1998). This zone is characterized by a lack of the parallel spreading corrugations that are observed further to the SW (Fig. 1; Ohara et al., 2003a). A total of 139 samples were obtained from this site during cruise KR03-01 aboard R/V *Kairei*, including 9 basaltic rock samples, 59 gabbroic samples, and 71 ultramafic samples.

The retrieved gabbro samples are generally altered and hydrated. We selected 9 of the 59 gabbroic samples, ranging in size from cobble-sized samples to granules for detailed microstructural and petrological analyses; the selected samples display visible structures such as mylonitic foliation (Table 1). Microstructures were analyzed in thin sections oriented perpendicular to the foliation and parallel to the lineation (XZ sections).

4. Microstructure

Microstructures were studied by both optical microscopy and scanning electron microscopy (JEOL JSM6300 SEM) at Shizuoka University, Japan. The studied samples are characterized by porphyroclastic textures consisting dominantly of plagioclase porphyroclasts and lesser clinopyroxene porphyroclasts in a fine-grained matrix of

134   plagioclase and amphibole. The samples can be classified into three types based on the

135   sizes of fine-grained plagioclase in the matrix: coarse, medium, and fine (Figs. 2a, c, e,

136   3; Table 1). As described below, each of the three sample types has distinctive

137   microstructural and chemical characteristics.

138   The four coarse-type samples (Figs. 2a, b, 4a, b; Table 1) are Fe-Ti oxide gabbro,

139   consisting of plagioclase, clinopyroxene, amphibole (brown and green hornblende),

140   ilmenite, magnetite and apatite (apatite was only observed in sample D6-1003). The

141   mean grain sizes of fine-grained plagioclase in the matrix vary between 80 and 130μm

142   (Fig. 3; Table 1). These samples contain moderately developed foliations defined by

143   alternating layers of plagioclase and clinopyroxene/amphibole. Plagioclase

144   porphyroclasts (~3mm) show features of intracrystalline deformation such as undulose

145   extinction, deformation twinning, and the formation of subgrains (Fig. 2b); no

146   compositional zoning is observed within these plagioclase porphyroclasts. Fine

147   plagioclase grains in the matrix are polygonal and occur dominantly around the

148   plagioclase porphyroclasts. These grains show features of intracrystalline deformation

149   such as undulose extinction and deformation twinning (Fig. 2b). Clinopyroxene grains

150   show undulose extinction and grain-size reduction, and secondary amphibole occurs as

151   both brown and green hornblende. It is important to note that although amphibole grains

152   commonly occur at the rims of clinopyroxene grains (Fig. 4a), they show no evidence of

153   deformation (Fig. 4b). This point is discussed further below.

154   The two medium-type samples are Fe-Ti oxide gabbro, consisting of plagioclase,

155   clinopyroxene, amphibole (brown and green hornblende), ilmenite, magnetite, and

156   apatite (Figs. 2c, d, 4c, d; Table 1). The mean grain sizes of plagioclase grains in the

157   matrix are approximately 25μm (Fig. 3; Table 1). These samples contain foliations

158   defined by alternating layers of plagioclase and clinopyroxene/amphibole. Plagioclase

159   porphyroclasts (~2mm) show features of intracrystalline deformation such as undulose

160   extinction and subgrains (Fig. 2d) with no evidence of compositional zoning. Fine

161   plagioclase grains in the matrix are polygonal and occur dominantly around plagioclase

162   porphyroclasts. Brown hornblende occurs as both porphyroclasts and fine grains (Fig.

163   4c): the porphyroclasts show features of intracrystalline deformation such as undulose

164   extinction, whereas the fine grains are equigranular and polygonal in shape (Fig. 4d).

165   The green hornblende mainly occurs at the rims of clinopyroxene and brown hornblende,

166   and, in contrast to the microstructures in brown hornblende, shows little evidence of

167   deformation. Locally, thin chlorite veinlets within the medium-type samples cut across

168   all other microstructures.

169   The three fine-type samples consist of plagioclase, amphibole (brown and green

170   hornblende), ilmenite, magnetite, and apatite (Figs. 2e, f, 4e, f; Table 1), making them

171   amphibolites. They contain only minor plagioclase and brown hornblende

172   porphyroclasts, and display a well-developed foliation defined by thin monomineralic

173   layers of either fine-grained plagioclase (gray layer in Fig. 2e) or brown hornblende

174 (brown layer in Fig. 2e) and mixed layers of these minerals. The plagioclase
175 porphyroclasts (~2mm) show features of intracrystalline deformation such as undulose
176 extinction and dynamic recrystallization (Fig. 2f). Compositional zoning is evident in
177 several plagioclase porphyroclasts. The fine plagioclase grains are as small as 8μm (Fig.
178 3; Table 1) and are approximately polygonal in shape. The brown hornblende
179 porphyroclasts show σ-type asymmetries (Fig. 4e; e.g., Passchier and Trouw, 2005).
180 Some fine-grained (~20μm) brown hornblende porphyroclasts show evidence of
181 compositional zoning, which may indicate anisotropic grain growth (Fig. 4e). The
182 brown hornblende porphyroclasts also show features of intracrystalline plasticity such
183 as undulose extinction and subgrain boundaries (Figs. 4e, f).
184
185 **5. Mineral chemistry**
186 Analyses of the chemistry of plagioclase, clinopyroxene, and amphibole grains in
187 polished XZ thin sections were undertaken using a JEOL JCXA-733 electron
188 microprobe at Shizuoka University, Japan, and a JEOL JXA-8200 electron microprobe
189 at the University of Tokyo, Japan. Operating conditions were as follows: probe current
190 of 12 nA, accelerating voltage of 15 kV, and correction procedure after Bence and Albee
191 (1968). Mineral compositions of peridotite and gabbro samples from the Godzilla
192 Mullion have been described previously in Ohara et al. (2003b). In the present study, we
193 present the mineral chemistry of the deformed gabbroic samples, as described above.
194 Plagioclase porphyroclasts have similar anorthite contents (An) in all samples,
195 ranging from An 40 to An 50. In the coarse-type samples, plagioclase porphyroclasts
196 and fine grains share the same range in composition (An 40–50; Fig. 5; Table 2). In the
197 medium-type samples, however, the compositions of fine-grained plagioclases are
198 different from those in coarse-type samples (An 30–40; Fig. 5; Table 2). The fine-type
199 samples show contrasting compositions between porphyroclasts and fine grains (An
200 20–30; Fig. 5; Table 2).
201 Coarse-type and medium-type samples have similar clinopyroxene compositions
202 (Table 3). The Mg/(Mg+Fe) number of clinopyroxene is 0.64–0.67 (Table 3); the
203 fine-type samples contain no clinopyroxene. The composition of amphibole in all three
204 sample types varies from pargasitic hornblende (i.e., brown hornblende) to actinolite
205 (i.e., green hornblende; Fig. 6a; Table 4); a plot of Al^{iv} vs. Al^{vi} + Ti + Fe^{3+} + A-site
206 occupancy shows an approximately linear correlation (Fig. 6b).
207
208 **6. Crystal-preferred orientation**
209 Crystal-preferred orientation (CPO) data for plagioclase and brown hornblende
210 were measured from highly polished XZ thin sections using a JEOL JSM6300 SEM
211 equipped with electron back-scattered diffraction (EBSD) at Shizuoka University, Japan.
212 Operating conditions were as follows: accelerating voltage of 20 kV, probe current of
213 10 nA, working distance of 24 mm, and specimens tilted at 70°. We measured the

214 crystal orientations of 201–281 plagioclase grains and 99–253 hornblende grains per
215 sample, visually checking the computerized indexation of each diffraction pattern. All
216 index data represent points with a mean angular deviation (MAD) of <1°. The measured
217 plagioclase and hornblende CPOs (Fig. 7) are presented on equal area, lower
218 hemisphere stereographic projections in the structural (X, Y, Z) reference frame.
219 Foliation (XY plane) is vertical, striking E–W, and the lineation (X direction) is
220 horizontal, trending E–W.

221   For plagioclase CPO data, the coarse-type samples show an alignment of [100]
222 subparallel to the lineation and a dominant alignment of (010) subparallel to the
223 foliation (Fig. 7a). One sample (D6-1009) shows an alignment of [100] parallel to the
224 lineation and a girdle distribution of (010) poles perpendicular to the lineation. The
225 medium-type samples show an alignment of [100] subparallel to the lineation and a
226 girdle distribution of poles to (010) planes perpendicular to the lineation (Fig. 7a). For
227 one coarse-type and one medium-type sample, we separately analyzed the CPOs of both
228 plagioclase porphyroclasts and fine grains to test for differences in deformation
229 mechanisms between them (e.g., Kruse et al., 2001): the two sets of grains show similar
230 CPO patterns (Fig. 8).

231   Plagioclase CPO patterns for two fine-type samples (D6-501 and D6-505) show
232 weak girdle distributions of [100] subparallel to the foliation and a weak alignment of
233 (001) within the plane of the foliation, whereas one fine-type sample (D6-502) shows a
234 random pattern (Fig. 7a). Within that sample (D6-502), we separately analyzed the
235 plagioclase CPO in both the monomineralic layer and the mixed layer in order to
236 investigate if there is any difference of deformation mechanism between them: both
237 layers show random orientations (Fig. 8).

238   CPO data for undeformed hornblende in a coarse-type sample reveal a weak
239 pattern, with (100) subparallel to the foliation and [001] lying within the plane of the
240 foliation (Fig. 7b). The two medium-type samples show alignments of [001] parallel to
241 the lineation and weak girdle distributions of poles to (100) perpendicular to the
242 lineation (Fig. 7b). Hornblende CPO patterns are most strongly developed in the
243 fine-type samples, being characterized by an intense alignment of [001] parallel to the
244 lineation and a distribution of (100) planes parallel to the foliation (Fig. 7b). For one
245 fine-type sample (D6-502), we separately analyzed the hornblende CPO in a
246 monomineralic hornblende layer and a mixed layer: the two sets of grains show the
247 similar (100)[001] CPO patterns (Fig. 9).

248

249 **7. Interpretation and discussion**
250 **7.1. Petrogenesis and retrograde metamorphism**
251   Both the coarse- and medium-type samples are amphibole-bearing Fe-Ti oxide
252 gabbros with amphibole, as described above. In comparing mineral compositions
253 between the coarse- and medium-types, clinopyroxene grains have similar Mg/(Mg+Fe)

254 values (Table 3), and plagioclase porphyroclasts have similar compositions (An 40–50;
255 Fig. 5). Because the plagioclase porphyroclasts rather than the fine-grained plagioclase
256 are likely to represent primary compositions (see Fig. 5), the similar compositions of
257 both clinopyroxene and plagioclase porphyroclasts in the two sample types suggest that
258 they were originally derived from the one gabbroic body. Since amphiboles in both the
259 coarse and medium types are of secondary rather than igneous origin (based on their
260 microstructural occurrence), we argue that hydrothermal alteration resulted in retrograde
261 metamorphism associated with deformation of the Fe-Ti oxide gabbroic body.

262 The fine-type samples are amphibolites; however, the mineral assemblages are
263 identical to those in both the coarse- and medium-types, except for clinopyroxene. It is
264 important to note that the compositions of plagioclase porphyroclasts and amphibole in
265 the fine-type samples are also comparable with those in the coarse and medium types
266 (Figs. 5, 6). This finding suggests that the amphibole grains in the fine-type samples are
267 the product of retrograde metamorphism that resulted from hydrothermal alteration of
268 the gabbroic body, as proposed for the coarse- and medium-types.

269 Plagioclase compositions are similar for porphyroclasts in the three sample types
270 (i.e., An 40–50), but the compositions of fine grains in the matrix are An 40–50 in the
271 coarse-type, An 30–40 in the medium-type, and An 5–30 in the fine-type (Fig. 5). In the
272 present study, the mineral assemblages in all three sample types contain plagioclase
273 (transformed from calcic plagioclase to sodic plagioclase), clinopyroxene (except for
274 the fine-type samples), amphibole (transformed from pargasitic hornblende to actinolite),
275 ilmenite, magnetite and apatite. During retrograde metamorphism, magmatic
276 plagioclase is generally recrystallized into more sodic plagioclase according to the
277 following reaction (Spear, 1981): clinopyroxene + plagioclase (calcic plagioclase) +
278 Fe-Ti oxide + fluid $\rightarrow$ magnesio-hornblende + plagioclase (sodic plagioclase). Indeed,
279 the modal composition of amphibole increased from the coarse-type samples, the
280 medium-type samples to the fine-type samples, whereas clinopyroxene disappeared in
281 the fine-type samples (Table. 1). Therefore, this reaction could be responsible for the
282 transformation of this gabbroic body into amphibolite (e.g., Berger et al., 2005).

283 The chemical compositions of amphibole grains depend on the pressure and/or
284 temperature at the time of retrograde reaction (Fig. 6; Spear, 1981). The temperature
285 sensitivity of amphibole can be estimated from a plot of Al^{iv} vs. $Al^{vi} + Ti + Fe^{3+} +$ A-site
286 occupancy (Brown, 1977; Spear, 1981; Díaz Asprioz et al., 2007). Indeed, our results
287 show that the composition of amphibole grains analyzed in the present study was
288 sensitive to temperature (Fig. 6b) and a decrease in Tschermakite components observed
289 in Fig. 6b. This suggests decreasing temperature, with the compositions of early and
290 later-stage amphibole corresponding to pargasitic hornblende and actinolite,
291 respectively.

292 We applied the hornblende–plagioclase geothermometer of Holland and Blundy
293 (1994) to brown hornblende and plagioclase within the three sample types, as shown in

Fig. 10. We assumed pressure conditions from 1kbar to 3kbar that corresponding to 5–10 km of depth within typical common oceanic crust. We chose pairs of matrix plagioclase (An 40–50) and undeformed brown hornblende (pargasitic hornblende) in coarse-type samples. The calculations yield a temperature range between 650 and 850 °C, with an average of approximately 750 °C (Fig. 10a). This suggests that the hydrothermal alteration recorded in the coarse-type samples occurred at temperatures of up to 800 °C. For the medium-type samples, we chose pairs of matrix plagioclase (An 30–40) and fine-grained brown hornblende (magnesio-hornblende), yielding temperature estimates in the range of 700–800 °C (Fig. 10b). Applying the hornblende–plagioclase geothermometer to a mixed layer of amphibole (magnesio-hornblende) and plagioclase (An 20–30) within a fine-type sample, we obtained distinctly lower temperature estimates, in the range of 560–775 °C (Fig. 10c). Consequently, we propose that the deformed rocks of all three sample types at site D6 were originally derived from a single gabbroic body, and have suffered retrograde metamorphism induced by hydrothermal activity at temperatures of 850–560 °C.

7.2. Timing of deformation with respect to retrograde metamorphism

All three sample types are characterized by porphyroclastic textures consisting dominantly of plagioclase porphyroclasts in a fine-grained matrix. Such deformation microstructures are typical of mylonite and ultramylonite within ductile shear zones. In contrast, microstructures within amphibole vary markedly among the three sample types.

In the coarse-type samples, secondary brown and green hornblende that replaced clinopyroxene show no evidence of deformation, in contrast to intensely deformed plagioclase and clinopyroxene grains (Figs. 2, 4). Furthermore, the compositions of fine-grained plagioclase in the matrix (An40–50) are similar to that of the plagioclase porphyroclasts (An 40–50). This trend indicates that deformation of the coarse-type samples occurred before hydration alteration, as hydration reactions would have changed the plagioclase composition. These observations provide clear evidences that hydrothermal alteration postdated the deformation event recorded in the coarse-type samples; therefore, the primary deformation would have occurred within the gabbroic body under anhydrous conditions at temperatures above 850°C (Fig. 10a), before the growth of amphibole during hydrothermal activity.

In the medium-type samples, secondary brown hornblende shows deformation features such as undulose extinction and subgrain boundaries (Fig. 4), whereas the secondary green hornblende is undeformed. This observation indicates that high-temperature hydrothermal alteration was synchronous with the deformation, with the low-temperature hydrothermal alteration postdating the deformation recorded in the medium-type samples. We therefore argue that subsequent to the first anhydrous stage under anhydrous conditions, the medium-type samples was deformed under hydrous

334   conditions at temperatures as high as 800 °C (Fig. 10b).

335   In the fine-type samples, secondary brown hornblende occurs as relatively small
336   porphyroclasts and within the fine-grained matrix. Secondary green hornblende occurs
337   at the grain boundaries of brown hornblende (Figs. 2, 4). These observations suggest
338   that although the fine-type samples appear to have been deformed at temperatures as
339   high as 775 °C (Fig. 10c), they continued to be deformed until the rock encountered
340   conditions at which green hornblende was able to grow, possibly at temperatures as low
341   as 560 °C (Fig. 10c).

342   We classified our deformed samples into three types based on the grain sizes of
343   fine-grained matrix plagioclase (Fig. 3). It is generally accepted that the size of
344   dynamically recrystallized grains is a function of flow stress during deformation (e.g.,
345   Michibayashi, 1993; Passchier and Trouw, 2005), with fine grain-sizes forming under
346   higher flow stresses at relatively low temperatures. Plagioclase porphyroclasts in all
347   three sample types show features of intracrystalline deformation such as undulose
348   extinction and subgrain boundaries (Fig. 2). Furthermore, the observed decrease in the
349   grain size of matrix plagioclase is consistent with the observed reduction in anorthite
350   composition (Fig. 11). Therefore, we argue that the fine-grained matrix plagioclase
351   dominantly resulted from the dynamic recrystallization of coarser plagioclase grains
352   during cooling of the gabbroic body. Consequently, we interpret the three sample types
353   to represent the progressive deformation of a single gabbroic body under decreasing
354   temperature (i.e., progressive retrogression).

355

356   **7.3. Deformation mechanism of plagioclase**

357   CPO patterns have traditionally been used to assess which slip systems were
358   active during dislocation creep in plastically deformed rock materials (e.g., Nicolas and
359   Poirier 1976; Wenk, 1985; Passchier and Trouw, 2005). In the coarse-type samples of
360   the present study, the observed plagioclase CPO pattern for both porphyroclasts and
361   matrix grains is consistent with the well described (010)[100] slip system (Figs. 7, 8a;
362   e.g., Montardi and Mainprice, 1987; Kruhl, 1987; Ji and Mainprice, 1988; Kruse et al.,
363   2001; Rosenberg and Stünitz, 2003), suggesting that dislocation creep was the dominant
364   deformation mechanism for plagioclase.

365   Similarly, because the microstructures in medium-type samples are also
366   dominated by intracrystalline deformation and comparable plagioclase CPO patterns
367   were obtained for porphyroclasts and matrix grains, dislocation creep might have been
368   the dominant deformation mechanism in these samples (Figs. 7, 8b). However, the CPO
369   patterns of the medium-type samples are slightly different from those of the coarse-type
370   samples, comprising an intense alignment of [100] subparallel to the lineation and a
371   weak girdle of both (010) and (001) poles subperpendicular to the lineation. These
372   patterns are consistent with the activation of (010)[100] and (001)[100] slip systems in
373   these samples.

374   The fine-type samples are dominated by a fine-grained matrix and plagioclase
375 porphyroclasts; the matrix consists of mixed layers and monomineralic layers. Because
376 the fine-type samples resulted from intense amphibolitization, it is unclear whether
377 plagioclase grains in the fine-grained matrix formed via the dynamic recrystallization of
378 originally coarse plagioclase grains; however, as some plagioclase porphyroclasts
379 contain dynamically recrystallized grains (Fig. 2f), in these cases there is no difference
380 in grain size between the fine-grained matrix and the dynamically recrystallized grains
381 around porphyroclasts. Therefore, we argue that at least some of the plagioclase grains
382 in the matrix were derived from dynamic recrystallization, indicating that dislocation
383 creep remained active at lower temperatures in these samples. In fact, the plagioclase
384 CPO patterns obtained for two samples (D6-501 and D6-505 in Fig. 7) suggest the
385 dominance of weak dominant (001)[100] slip. It must also be emphasized that a
386 decrease in grain size enhances the activity of grain-size-dependent deformation
387 mechanisms such as diffusion creep and grain boundary sliding (e.g., Jiang et al., 2000;
388 Passchier and Trouw, 2005; Warren and Hirth, 2006). Therefore, the strong grain-size
389 reduction (8µm) observed in the matrix within the fine-type samples may have enabled
390 grain-size-sensitive creep at the time when dislocation creep remained active. In fact,
391 the plagioclase CPO pattern for one of the fine-type samples (D6-502 in Fig. 7a) shows
392 a very weak or random pattern, with both the mixed and monomineralic layers showing
393 a highly scattered CPO (D6-502 in Fig. 8); these observations indicate that
394 grain-size-sensitive creep (e.g. Warren and Hirth, 2006) could have been the dominant
395 deformation mechanism in this sample.
396
397 **7.4. Deformation mechanism of amphibole**
398   Various deformation mechanisms have been reported for amphibole, including
399 (−101) mechanical twinning (e.g., Rooney et al., 1975), dynamic recrystallization with
400 dislocation creep and fracturing (e.g., Hacker and Christie, 1990), and brittle behavior
401 with minor solution mass transfer and dissolution-precipitation creep (e.g., Imon et al.,
402 2004). Rigid body rotation is also considered to play an important role in CPO
403 development in clinoamphibole (e.g., Díaz Aspiroz et al., 2007).
404   In the coarse-type samples of the present study, brown and green hornblende
405 shows no evidence of plastic deformation (Fig. 4b); therefore, the measured CPO
406 pattern is considered to have formed during hydrothermal alteration (Fig. 7b). Brown
407 hornblende grains in the medium-type samples show intracrystalline deformation,
408 without anisotropic grain growth or compositional zoning (Fig. 4e, f); these features are
409 indicative of plastic deformation. The CPO patterns of brown hornblende show
410 alignments of [001] parallel to the lineation and a weak distribution of (100) planes
411 within the plane of the foliation (Fig. 7b), consistent with activation of the (100)[001]
412 slip system (e.g., Díaz Asprioz et al., 2007). Therefore, the deformation mechanism of
413 brown hornblende is likely to have been dominated by dislocation creep.

414   In contrast to the weak CPO patterns in plagioclase, the fine-type samples tend to
415   record intense amphibole CPO patterns (Fig. 7). We found a few evidences of
416   anisotropic grain growth and compositional zoning in brown hornblende (Fig. 4e), but
417   also undulose extinction and subgrain boundaries (Figs. 4e, f). However, the possibility
418   of dissolution-precipitation creep is probably very low, as this generally occurs at
419   relatively low temperatures such as those of the greenschist facies to lower amphibolite
420   facies (e.g., Imon et al., 2004). In contrast, the samples studied here were deformed
421   within the upper amphibolite facies or at higher grades (e.g., Fig. 10), as discussed
422   above. Therefore, it may be likely that the dominant deformation mechanism was
423   dislocation creep via (100)[001] slip, although we cannot exclude the other deformation
424   mechanisms such as dissolution-precipitation creep. A more detailed study on the
425   deformation mechanisms of amphibole is required in the future.
426
427   **7.5. Significance of a gabbroic shear zone within the Godzilla Mullion**
428   Given that the three sample types were probably derived from the same gabbroic
429   body, each type is interpreted to represent a different stage of deformation during
430   progressive retrogression. Plagioclase appears to exhibit a change in deformation
431   mechanism from dislocation creep in the coarse- and medium-types to
432   grain-size-sensitive creep in the fine-type, as grain size decreases with decreasing
433   temperature. Thus, the fine-type samples are inferred to represent the final stage of
434   ductile deformation along a shear plane that possibly extended upward to a detachment
435   fault at shallow levels in the crust.   Furthermore, since hydrothermal alteration within
436   the fine-type samples is more than that within the coarse- and medium-type samples, we
437   argue that the hydration was preferentially localized within the shear zone.
438   The fault rocks exposed at the surface of the Godzilla Mullion are mainly material
439   derived from the deep oceanic lithosphere, such as gabbro and peridotite (Ohara et al.,
440   2003b; Harigane et al., 2005). Because these fault rocks also include talc schist,
441   indicative of low-temperature deformation, they are thought to represent a detachment
442   fault within the Parece Vela Rift (Harigane et al., 2005) such as that within the
443   Mid-Atlantic Ridge 15º45'N in discussed MacLeod et al. (2002) and Escartin et al.
444   (2003). In this paper, we propose that samples of Fe-Ti oxide gabbro dredged from site
445   D6 were deformed during progressive retrogression, probably related to uplift of the
446   gabbroic body.
447   The dredged site, D6, is located ~15 km from the breakaway area, the distal end
448   of the Godzilla Mullion (Fig. 1). Tucholke et al. (1998) proposed that the breakaway
449   fault is likely to cut through the entire crust and extend into the upper mantle. Indeed,
450   the nature of the deformed gabbroic rocks from site D6 suggests that they are possibly
451   mylonitic gabbros derived from a shear zone(s) related to the initial detachment faulting
452   associated with the development of the Godzilla Mullion. Among mylonitic peridotites
453   and gabbros sampled from or near the surface of OCCs (e.g., Dick et al., 1991; Cannat

454 et al., 1992; Jaroslow et al., 1996; Agar and Lloyd, 1997; Karson, 1999; Schroeder and

455 John, 2004), mylonites of highly evolved Fe-Ti oxide-rich gabbro at Atlantis Bank,

456 adjacent to the Atlantis II transform and ~90 km south of the active Southwest Indian

457 Ridge, are regarded as a direct link to a detachment fault (Dick et al., 1991, 2000).

458   Consequently, in the context of the present study, the development of a shear zone

459 related to the initiation of a detachment fault might have occurred according to the

460 following steps (Fig. 12). (1) An Fe-Ti oxide gabbro body was initially sheared at

461 temperatures above 850 °C under anhydrous conditions and subsequently subjected to

462 alteration at around 650 °C, resulting in the formation of the coarse-type samples in

463 high-temperature shear zones as described above (Fig. 12a). These samples could

464 represent the primary shear zone associated with the detachment fault developed within

465 the Godzilla Mullion. (2) The shear zone subsequently developed under hydrous

466 conditions with decreasing temperature, possibly associated with uplift of the gabbro

467 body, resulting in formation of the medium-type samples in progressively narrower

468 mylonitic zones (Fig. 12b). (3) The shear zone was further influenced by hydrothermal

469 alteration under retrogressive conditions and temperatures as low as 560 °C during

470 uplift of the gabbro body, resulting in the amphibolitization evident in the fine-type

471 samples (Fig. 12c). Because the fine-type samples are microstructurally ultramylonitic

472 amphibolites (Figs. 2, 4), and because they record a wide range of temperatures

473 (560–850 °C; Fig. 10c), it is possible that intense shear localization (i.e. progressive

474 narrowing of mylonitic zones overprinting high-temperature shear zones) occurred in

475 association with hydrothermal activity in the primarily high-temperature shear zone (Fig.

476 12). Thus, the fine-type samples are inferred to represent the last stage of ductile

477 deformation within the Fe-Ti oxide gabbro body, along the slip plane associated with

478 the detachment fault in the Godzilla Mullion. Alternatively, they could represent a

479 deformation event related to emplacement of the gabbros at depth, being unrelated to

480 the detachment fault. Therefore, the above model requires further testing via further

481 structural studies of deformed rocks dredged from various parts of the Godzilla Mullion .

482 Nonetheless, the results of this study suggest that the surface geology of the Godzilla

483 Mullion is consistent with an OCC capped by a deep-rooted detachment fault, and that

484 the involvement of gabbros in the structural development of the Godzilla mullion—in a

485 similar way to that described at the Atlantis Bank in the Southwest Indian Ridge (Dick

486 et al., 2000) —is consistent with the working hypothesis that large gabbro intrusions are

487 always associated with OCC development (Ildefonse et al., 2007).

488

489 **8. Conclusions**

490   (1) Dredge samples of gabbroic rock collected from near the breakaway of the

491 Godzilla Mullion (dredge site D6) contain microstructures indicative of intense ductile

492 deformation, characterized by porphyroclastic textures dominantly of plagioclase

13

493 porphyroclasts and lesser clinopyroxene porphyroclasts in a fine-grained matrix.

494   (2) Samples are classified into the three types based upon the grain size of
495 fine-grained plagioclase in the matrix: coarse (80–130μm), medium (25μm), and fine
496 (~10μm). Although the chemical composition of plagioclase porphyroclasts is
497 consistently An 40–50 among all three sample types, the compositions of fine grains in
498 the matrix vary with grain size, being An 40–50 for the coarse-type, An 30–40 for the
499 medium-type, and An 5–30 for the fine-type. This finding implies that the chemical
500 composition of plagioclase in the matrix is related to the following syn-deformation
501 retrograde reaction: clinopyroxene + plagioclase + Fe-Ti oxide + fluid $\rightarrow$ hornblende +
502 plagioclase.

503   (3) Plagioclase crystal-preferred orientations show a gradual change from a
504 (010)[100] pattern in coarse-type samples, (010)[100] and (001)[100] patterns in
505 medium type, and a weak (001)[100] pattern or random orientations in fine type. This
506 variation in CPO pattern resulted from a change in the deformation mechanism of
507 plagioclase from dislocation creep to grain-size-sensitive creep with decreasing
508 temperature, thereby leading to strain localization during cooling.

509   (4) Within each of the sample types, the composition of amphibole varies from
510 pargasitic hornblende to actinolite. Amphibole in the coarse type shows no evidence of
511 deformation, meaning that it postdates plagioclase deformation and recrystallization; in
512 contrast, brown hornblende in the medium- and fine-types are plastically deformed. The
513 dominant deformation mechanism could be dislocation creep via (100)[001] slip.

514   (5) The microstructural development of the gabbroic rocks occurred during
515 uplift-related cooling of the gabbro body, and a primary shear zone developed at the
516 breakaway zone at depth under anhydrous conditions at high temperatures above 850 °C.
517 The shear zone subsequently evolved during progressive retrogression in association
518 with hydration, possibly resulting in the development of the detachment fault that gave
519 rise to the Godzilla Mullion.

520

References

Agar, S. M. and Lloyd, G. E., 1997. Deformation of Fe-Ti oxides in gabbroic shear zones from the MARK area, Proc. Ocean Drill. Program, Sci. Results, 153, 123-141.

Bence, A. E., Albee, A. L., 1968. Empirical correction factors for the electron microanalysis of silicates and oxides. J. Geol., 76, 382-403.

Berger, J., Femenias, O., Mercier, J. C. C. and Demaiffe, D., 2005. Ocean-floor hydrothermal metamorphism in the Limousin ophiolite (western French Massif Central): evidence of a rare preserved Variscan oceanic marker. J. Metamorph. Geol., 23, 795-812.

Blackman, D. K., Cann, J. R., Janssen, B. and Smith, D. K., 1998. Origin of extensional core complexes: Evidence from the Mid-Atlantic Ridge at Atlantis Fracture Zone. J. Geophys. Res., 103, 21315-21333.

Brown, E. H., 1977. The crossite content of Ca-amphibole as a guide to pressure of metamorphism. J. Petrol., 18, 53-72.

Cann, J. R., Blackman, D. K., Smith, D. K., McAllister, E., Janssen, B., Mello, S., Avgerinos, E., Pascoe, A. R. and Escartin, J., 1997. Corrugated slip surfaces formed at ridge-transform intersections on the Mid-Atlantic Ridge. Nature, 385, 329-332.

Cannat, M., Bideau, D. and Bougault, H., 1992. Serpentinized peridotites and gabbros in the Mid-Atlantic Ridge axial valley at 15°37'N and 16°52'N, Earth Planet. Sci. Lett., 109, 87-106.

Christie, D. M., West, B. P., Pyle, D. G. and Hanan, B. B., 1998. Chaotic topography, mantle flow and mantle migration in the Australian–Antarctic discordance. Nature, 394, 637-644.

Díaz Asprioz, M., Lloyd, G. E. and Fernández, C., 2007. Development of lattice preferred orientation in clinoamphiboles deformed under low-pressure metamorphic conditions. A SEM/EBSD study of metabasites from the Aracena metamorphic belt (SW Spain). J. Struct. Geol., 29, 629-645.

Dick, H. J. B., Schouten, H., Meyer, P. S., Gallo, D. G., Bergh, H., R. Tyce, R., Patriat, P., Johnson, K. T. M., Snow, J. and Fischer, A., 1991. Tectonic evolution of the Atlantis II Fracture Zone, Proc. Ocean Drill. Program, Sci. Results, 118, 359-398.

Dick, H. J. B., Natlamd, J. H., Alt, J. C., Bach, W., Bideau, D., Gee, J. S., Haggas, S., Hertogen, J. G. H., Hirth, G., Holm, P. M., Ildefonse, B., Iturrino, G. J., John, B. E., Kelley, D. S., Kikawa, E., Kingdon, A., LeRoux, P. J., Maeda, J., Meyer, P. S., Miller, D. J., Naslund, H. R., Niu, Y., Robinson, P. T., Snow, J., Stephan, R. A., Trimby, P. W., Worm, H. and Yoshinobu, A., 2000. A long in situ section of the lower ocean crust: results of ODP Leg 176 drilling at the Southwest Indian Ridge, Earth Planet. Sci.

573   Lett., 179, 31-51.

574   Dick, H. J. B., Lin, J. and Schouten, H., 2003. An ultraslow-spreading class of ocean
575   ridge. Nature, 426, 405-412.

576   Escartin, J., Mevel, C., MacLeod, C. J. and McCaig, A. M., 2003, Constraints on
577   deformation conditions and the origin of oceanic detachments: The Mid-Atlantic
578   Ridge core complex at 15°45'N. Geochem. Geophys. Geosys., **4**(8) 1067,
579   doi:10.1029/2001GC000278.

580   Hacker, B. R. and Christie, J. M., 1990. Brittle/ductile and plastic/cataclastic transition
581   in experimentally deformed and metamorphosed amphibolite, in: Duba, A.G.,
582   Durham, W.B., Handin, J.W., Wang, H.F. (Eds.), The Brittle-Ductile Transition in
583   Rocks. AGU Geophysical Monograph., Washington, D.C., pp.127-148.

584   Harigane, Y., Michibayashi, K. and Ohara, Y., 2005. Detachment faulting at the
585   Godzilla Mullion, Parece Vela Basin, Philippine Sea. Eos Trans. AGU, 86 (52), Fall
586   Meet. Suppl., Abstr. T41D-1341.

587   Holland, T. J. B. and Blundy, J. D., 1994. Non-ideal interactions in calcic amphiboles
588   and their bearing on amphibole-plagioclase thermometry. Contrib. Mineral. Petrol.,
589   116, 433-447.

590   Ildefonse, J., Blackman, D. K., John, B. E., Ohara, Y., Miller, D. J., MacLeod, C. J. and
591   Integrated Ocean Drilling Program Expeditions 304/305 Science Party, 2007,
592   Oceanic core complexes and crustal accretion at slow-spreading ridges. Geology,
593   35(7), 623–626, doi: 10.1130/G23531A.

594   Imon, R., Okudaira, T. and Kanagawa, K., 2004. Development of shape- and
595   lattice-preferred orientations of amphibole grains during cataclastic deformation and
596   subsequent deformation by dissolution-precipitation creep in amphibolites from the
597   Ryoke metamorphic belt, SW Japan. J. Struct. Geol., 26, 793-805.

598   Jaroslow, G. E., Hirth, G. and Dick, H. J. B., 1996. Abyssal peridotite mylonites:
599   implications for grain-size sensitive flow and strain localization in the oceanic
600   lithosphere, Tectonophysics, 256, 17-37.

601   Ji, S. and Mainprice, D., 1988. Natural deformation fabrics of plagioclase: implications
602   for slip systems and seismic anisotropy. Tectonophysics, 47, 145-163.

603   Jiang, Z., Prior, D. J. and Wheeler, J., 2000. Albite crystallographic preferred
604   orientation and grain misorientation distribution in a low-grade mylonite:
605   implications for granular flow. J. Struct. Geol., 22, 1663-1674.

606   Karson, J. A., 1990. Seafloor spreading on the Mid-Atlantic Ridge: Implications for the
607   structure of ophiolites and oceanic lithosphere produced in slow-spreading
608   environments, in Ophiolites and Oceanic Crustal Analogues: Proceedings of the
609   Symposium "Troodos 1987", edited by J. Malpas et al., pp. 125-130, Geol. Surv.
610   Dept., Nicosia, Cyprus.

611   Karson, J. A., 1999. Geological investigation of a lineated massif at the Kane transform:
612   Implications for oceanic core complexes, Philos. Trans. R. Soc. London, Ser.

613   A, 357, 713-740.

614 Kasuga, S. and Ohara, Y., 1997. A new model of back-arc spreading in the Parece Vela
615   Basin, northwest Pacific margin. Is. Arc, 6, 316-326.

616 Kruhl, J. H. 1987. Preferred lattice orientations of plagioclase from amphibolite and
617   greenschist facies rocks near the Insubric Linc (Western Alps). Tectonophysics, 135,
618   233-242.

619 Kruse, R., Stünitz, H. and Kunze, K., □ 2001. Dynamic recrystallization process in
620   plagioclase porphyroclasts. J. Struct. Geol., 23, 1781-1802.

621 Kumagai, H., Okino, K., Joshima, M., Morishita, T., Nakamura, K., Neo, N., Okada, S.,
622   Sato, T., Sawaguchi, T., Shibuya, T., Takaesu, M. and Takai, K., 2006. A field-work
623   approach to investigate UltraH3-linkage hypothesis at two distinct hydrothermal
624   fields Indian Ocean. Eos Trans. AGU, 87(36), West. Pac. Geophys. Meet. Suppl.,
625   Abstract T41B-01.

626 Leake, B.E., Woolley, A. R., Arps, C. E. S., Birch, W. D., Gilbert, M. C., Grice, J. D.,
627   Hawthorne, F. C., Kato, A., Kisch, H. J., Krivovichev, V. G., Linthout, K., Laird, J.,
628   Mandrino, J., Maresch, W. V., Nickel, E. H., Rock, N. M. S., Schumacher, J. C.,
629   Smith, D. C., Stephenson, N. C. N., Ungaretti, L., Whittaker, E. J. W., and Youzhi,
630   G., 1997. Nomenclature of amphiboles: report of the subcommittee on amphiboles of
631   the international mineralogical association commission on new minerals and mineral
632   names. Am. Mineral., 82, 1019-1037.

633 MacLeod, C. J., Escartin, J., Banerji, D., Banks, G. J., Gleeson, M., Irving, D. H. B.,
634   Lilly, R. M., McClaig, A. M., Niu, Y., Allerton, S. and Smith, D. K., 2002, Direct
635   geological evidence for oceanic detachment faulting: The Mid-Atlantic Ridge,
636   15°45'N. Geology, 30, 879-882.

637 Martinez, F., J. Karsten, and E. M. Klein., 1998. Recent Kinematics and Tectonics of the
638   Chile Ridge, Eos Trans. AGU, 79, Fall Meetings Suppl., Abstract F836.

639 Michibayashi, K., 1993. Syntectonic development of a strain independent dynamically
640   recrystallized quartz grain during mylonitization. Tectonophysics, 222, 151-164.

641 Montardi, Y. and Mainprice, D., 1987. A TEM study of the natural plastic deformation
642   of calcic plagioclase. Bull. Mineral., 110, 1-14.

643 Nicolas, A. and Poirier, J. P., 1976. Crystalline Plasticity and Solid State Flow in
644   Metamorphic Rocks. Wiley, New York, 444pp.

645 Ohara, Y., Yoshida, T. and Kasuga, S., 2001. Giant megamullion in the Perece Vela
646   Backarc basin. Mar. Geophys. Res., 22, 47-61.

647 Ohara, Y., Okino, K. and Snow, J., KR03-01 Shipboard Scientific Party, 2003a.
648   Preliminary report of Kairei KR03-01 cruise: amagmatic tectonics and lithospheric
649   composition of the Parece Vela Basin. InterRidge News, 12(1), 27-29.

650 Ohara, Y., Fujioka, K., Ishii, T. and Yurimoto, H., 2003b. Peridotites and gabbros from
651   the Parece Vela backarc basin: Unique tectonic window in an extinct backarc
652   spreading   ridge.   Geochem.   Geophys.   Geosys.,   4(7),   1029,

653   doi:10.1029/2002GC000469.

654 Okino, K., Kasuga, S. and Ohara, Y., 1998. A new scenario of the Parece Vela Basin
655   genesis. Mar. Geophys. Res., 20, 21-40.

656 Okino, K., Ohara, Y., Kasuga, S. and Kato, Y., 1999. The Philippine Sea: New survey
657   results reveal the structure and the history of the marginal basins. Geophys. Res. Lett.,
658   26, 2287-2290.

659 Okino, K., Matsuda, K., Christie, D. M., Nogi, Y. and Koizumi, K., 2004. Development
660   of oceanic detachment and asymmetric spreading at the Australian-Antarctic
661   Discordance. Geochem. Geophys. Geosys., 5, Q12012, doi:10.1029/2004GC000793.

662 Passchier, C. W. and Trouw, R. A. J., 2005. Microtectonics, Second ed. Springer, New
663   York. 369pp.

664 Rooney, T.P., Riecker, E. R. and Gavasci, A.T., 1975. Hornblende deformation features.
665   Geology, 3, 364-366.

666 Rosenberg, C. L. and Stünitz, H., 2003. Deformation and recrystallization of plagioclase
667   along a temperature gradient: an example from the Bergell tonalite. J. Struct.
668   Geol., 25, 389-408.

669 Schroeder, T. and John, B. E., 2004. Strain localization on an oceanic detachment fault
670   system, Atlantis Massif, 30°N, Mid-Atlantic Ridge. Geochem. Geophys. Geosys.,
671   5(11), Q11007, doi:10.1029/2004GC000728.

672 Spear, F., 1981. An experimental study of hornblende stability and compositional
673   variability in amphibolite. Am. J. Sci., 281, 697-734.

674 Smith, D. K., Escartin, J., Schouten, H. and Cann, J. R., 2008, Fault rotation and core
675   complex formation: Significant processes in seafloor formation at slow-spreading
676   mid-ocean ridges (Mid-Atlantic Ridge, 13°–15°N). Geochem. Geophys. Geosys., 9
677   Q03003, doi:10.1029/2007GC001699.

678 Tucholke, B. E. and Lin, J., 1994, A geological model for the structure of ridge
679   segments in slow spreading ocean crust. J. Geophys. Res., 99, 11937-11958.

680 Tucholke, B. E., Lin, J. and Kleinrock, M. C., 1998. Megamullions and mullion
681   structure defining oceanic metamorphic core complexes on the Mid-Atlantic Ridge. J.
682   Geophys. Res., 103, 9857-9866.

683 Warren, J. M. and Hirth, G., 2006. Grain size sensitive deformation mechanisms in
684   naturally deformed peridotites. Earth. Planet. Sci. Lett., 248 423-435.

685 Wenk, H.R., 1985. Preferred Orientation in Deformed Metals and Rocks. An
686   Introduction to Modern Texture Analysis. Academic Press, New York.

687

Figure captions

689   Fig. 1. Left: Major bathymetric features of the Western Pacific Ocean (after Ohara et al.,
690   2001). The rectangle shows the location of the study area at the site of the
691   Godzilla Mullion, Parece Vela Basin. Right: Bathymetric map of the Godzilla
692   Mullion (outlined by dashed line), showing the location of dredge site D6 and
693   other dredge sites conducted during cruises KR03-01 and KH07-02-Leg2/Leg4.
694   The inactive spreading segments S1 and S2 (Ohara et al., 2001) are marked by
695   thick red lines.

696

697   Fig. 2. Photomicrographs of plagioclase microstructures within samples of mylonitic
698   gabbro (coarse, medium, and fine types) collected from the Godzilla Mullion.
699   (a) Plagioclase porphyroclast and matrix in a coarse-type sample (D6-1002). (b)
700   Enlargement of the area outlined by the yellow rectangle in (a). (c) Plagioclase
701   porphyroclast and matrix in a medium-type sample (D6-1005). (d) Enlargement
702   of the area outlined by the yellow rectangle in (c). (e) Plagioclase porphyroclast
703   and matrix in a fine-type sample (D6-502). The grayish layer mainly consists of
704   plagioclase grains (i.e. monomineralic plagioclase layer). The brownish layer
705   consists of amphibole grains (i.e. monomineralic amphibole layer). The mixed
706   layer is the area where both plagioclase (grayish color) and amphibole (brownish
707   color) are present. (f) Enlargement of the area outlined by the yellow rectangle
708   in (e). All images were taken under crossed nicols.

709

710   Fig. 3. Logarithmic grain-size distributions of fine-grained plagioclase grains. Outlines
711   of plagioclase grains were traced from photomicrographs and back-scattered
712   electron images, and shape parameters were measured using ImageJ software.
713   We measured a total of 113 to 645 plagioclase grains per sample. The gabbro
714   samples can be classified into three types based on the sizes of dynamically
715   recrystallized plagioclase grains: coarse-type (upper row; average grain size,
716   80–130 μm), medium-type (middle row; average grain size, 25 μ m), and
717   fine-type (lower row; average grain size, 8 μm). All of the distributions are
718   log-normal. Triangles indicate the average grain size within each sample.

719

720   Fig. 4. Photomicrographs of amphibole microstructures within samples of mylonitic
721   gabbro (coarse, medium, and fine types) collected from the Godzilla Mullion.
722   (a) Clinopyroxene grains are replaced by amphibole in a coarse-type sample
723   (D6-1002). Open nicols. (b) Enlargement of the area outlined by the yellow
724   rectangle in (a). Open nicols. (c) Clinopyroxene porphyroclast surrounded by
725   fine-grained amphibole grains in a medium-type sample (D6-1005). Open nicols.
726   (d) Enlargement of the area outlined by the yellow rectangle in (c). Crossed
727   nicols. (e) Amphibole porphyroclasts and matrix in a fine-type sample (D6-502).

728   Crossed nicols. The brown area is made up of brown hornblende grains. (f)
729   Crystal-preferred orientation map (data collected by EBSD) of brown
730   hornblende in the area outlined by the yellow rectangle in (e). The map was
731   collected at a 1μm step size, and is rotated 90° anticlockwise from the
732   orientation shown in (e), which is shown by yellow arrow. Color indicates Euler
733   axes. White points were unable to be indexed (i.e. zero solution). Black lines
734   indicate grain boundaries, defined as a 10° (or greater) misorientation between
735   adjacent points. Cyan and magenta lines indicate subgrain boundaries defined by
736   misorientation of 5° and 2°, respectively. Cpx: clinopyroxene, BHb: brown
737   hornblende, GHb: green hornblende, Pl: plagioclase.
738
739   Fig. 5. Chemical compositions of plagioclase porphyroclasts (small black diamonds)
740   and fine grains in the matrix (large white diamonds) for coarse, medium, and
741   fine sample types. Anorthite content is calculated as $Ca \times 100 / (Ca + Na + K)$.
742
743   Fig. 6. Chemical compositions of secondary amphibole within coarse-, medium-, and
744   fine-type samples. Estimates of cation contents and Fe^{3+} in all sample types were
745   made following Holland and Blundy (1994). (a) Plot of A-site occupancy vs. Si
746   content for amphibole within all three sample types. Terminology and
747   classification scheme are from Leake et al. (1997). (b) Plot of Al^{iv} vs. $Al^{vi} + Fe^{3+}$
748    $+ Ti + A$-site occupancy for amphibole within all three sample types. Increasing
749   values along the dashed line indicate broadly increasing temperature.
750
751   Fig. 7. Crystallographic-preferred orientation data for (a) plagioclase grains and (b)
752   amphibole grains in samples with coarse-type texture (D6-1001, D6-1002,
753   D6-1003, D6-1009), medium-type texture (D6-500, D6-1005), and fine-type
754   texture (D6-500, D6-502, D6-505). The measured plagioclase and hornblende
755   CPOs are presented on equal area, lower hemisphere projections in the structural
756   (XZ) reference frame. The data for hornblende grains in coarse-type samples are
757   sourced only from sample D6-1002 because of the small number of analyzed
758   grains in coarse-type samples. In all plots, the foliation is vertical (XY plane)
759   and the lineation (X) is horizontal within the plane of the foliation.
760
761   Fig. 8. Crystallographic-preferred orientation data for plagioclase grains in samples with
762   coarse-type texture (D6-1002), medium-type texture (D6-1005), and fine-type
763   texture (D6-502). The measured plagioclase CPOs are presented on equal area,
764   lower hemisphere projections in the structural (XZ) reference frame. Data for
765   coarse- and medium-type samples include both porphyroclasts (black squares)
766   and neoblasts (open squares). Data for fine-type samples include grains from
767   mixed layers (black squares) and monomineralic layers (open squares). In all

20

768   plots, the foliation is vertical (XY plane) and the lineation (X) is horizontal
769   within the plane of the foliation.
770

771 Fig. 9. Crystallographic-preferred orientation data for amphibole grains in a sample with
772   fine-type texture (D6-502). The data are presented on equal area, lower
773   hemisphere projections in the structural (XZ) reference frame, showing data for
774   both mixed layers (black squares) and monomineralic layers (open squares). The
775   foliation is vertical (XY plane) and the lineation (X) is horizontal within the
776   plane of the foliation.
777

778 Fig. 10. Temperatures estimated by applying the hornblende–plagioclase
779   geothermometer of Holland and Blundy (1994) to coarse- (D6-1002), medium-
780   (D6-1005), and fine-type samples (D6-502).
781

782 Fig. 11. Comparison of grain size and anorthite content for plagioclase matrix. The
783   grain size decreases with decreasing anorthite content.
784

785 Fig. 12. Schematic model of the progressive development of a shear zone in the
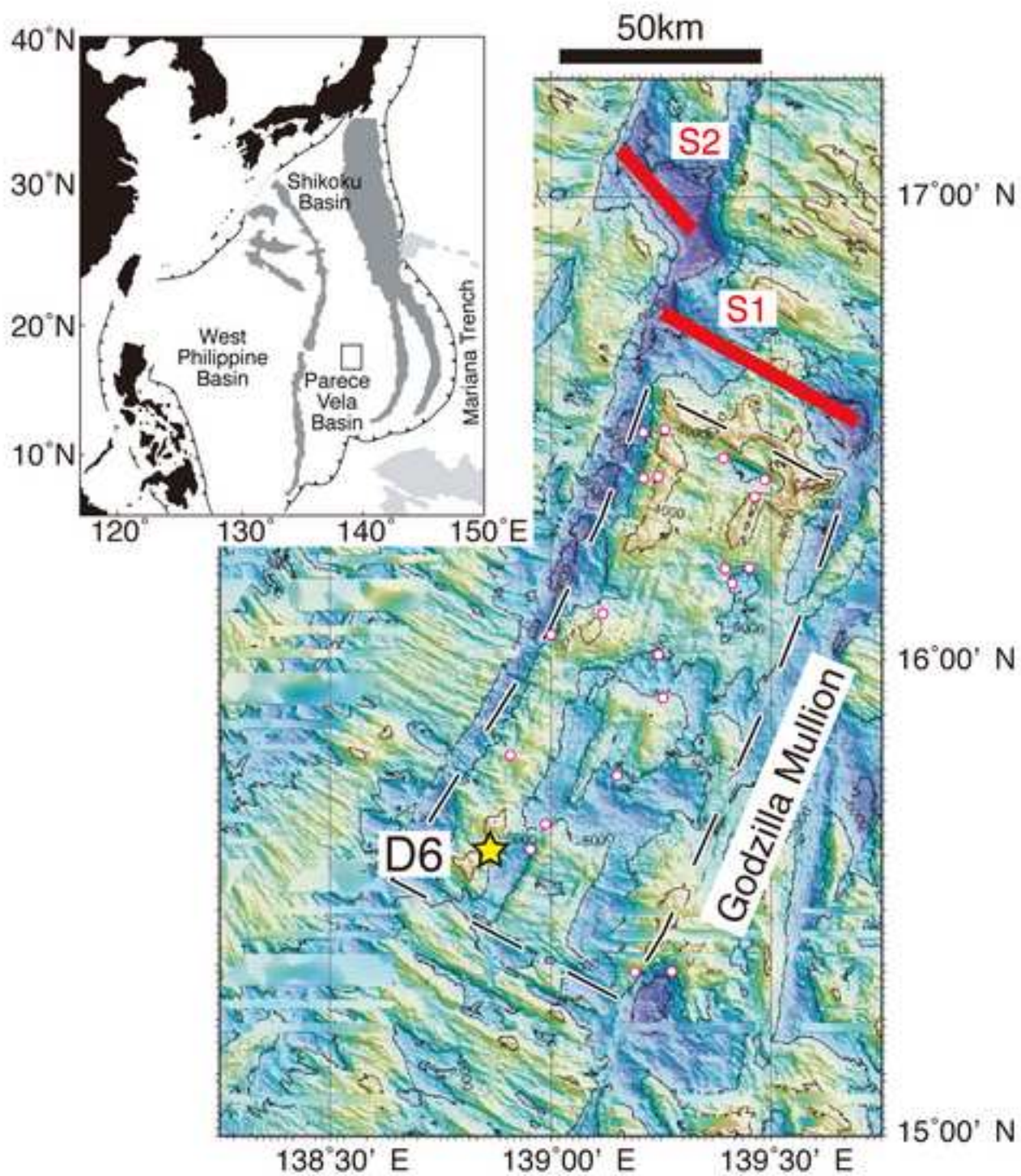786   Godzilla Mullion. See text for further details.
787

Figure 1

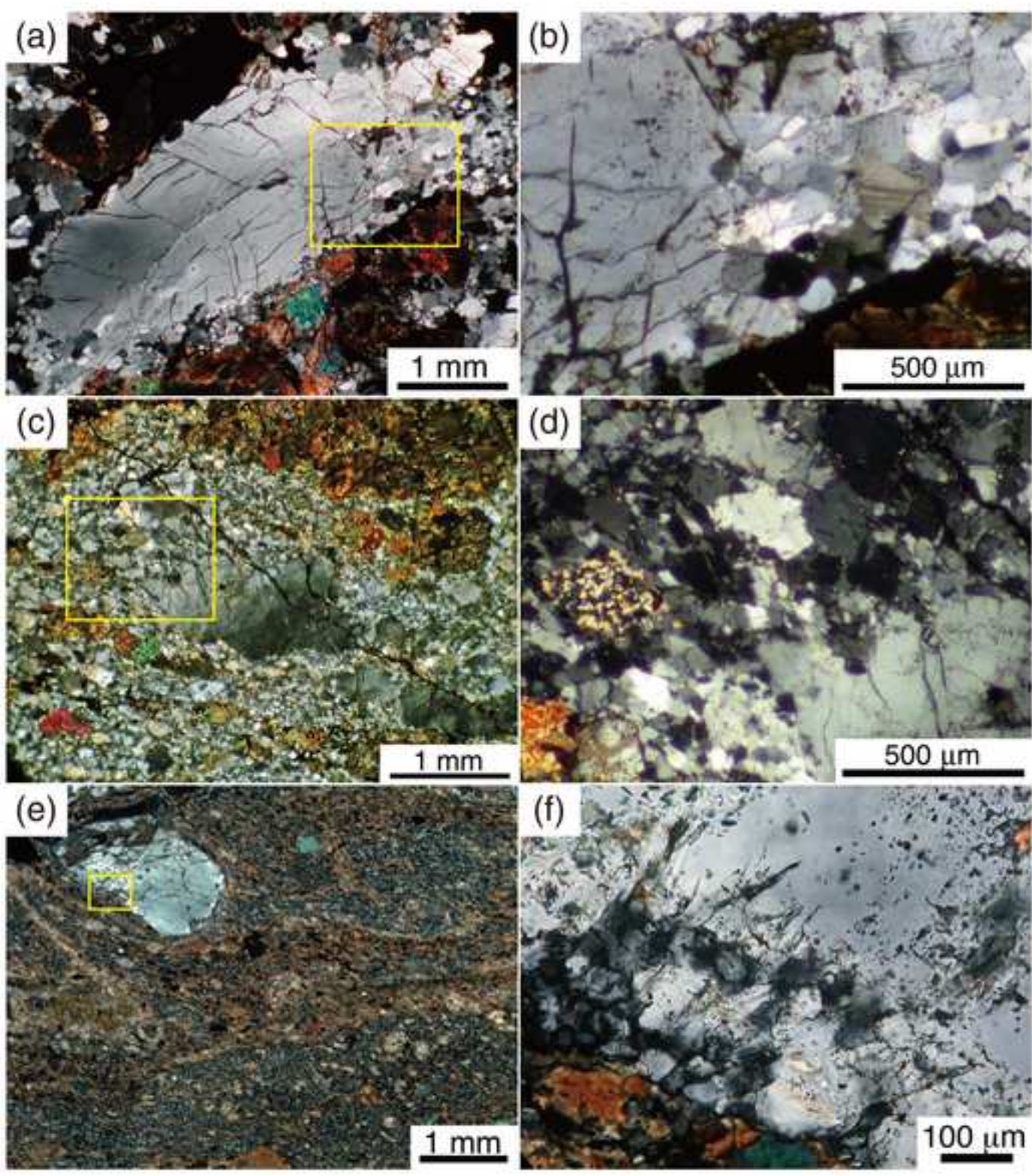Figure 1. Harigane et al.

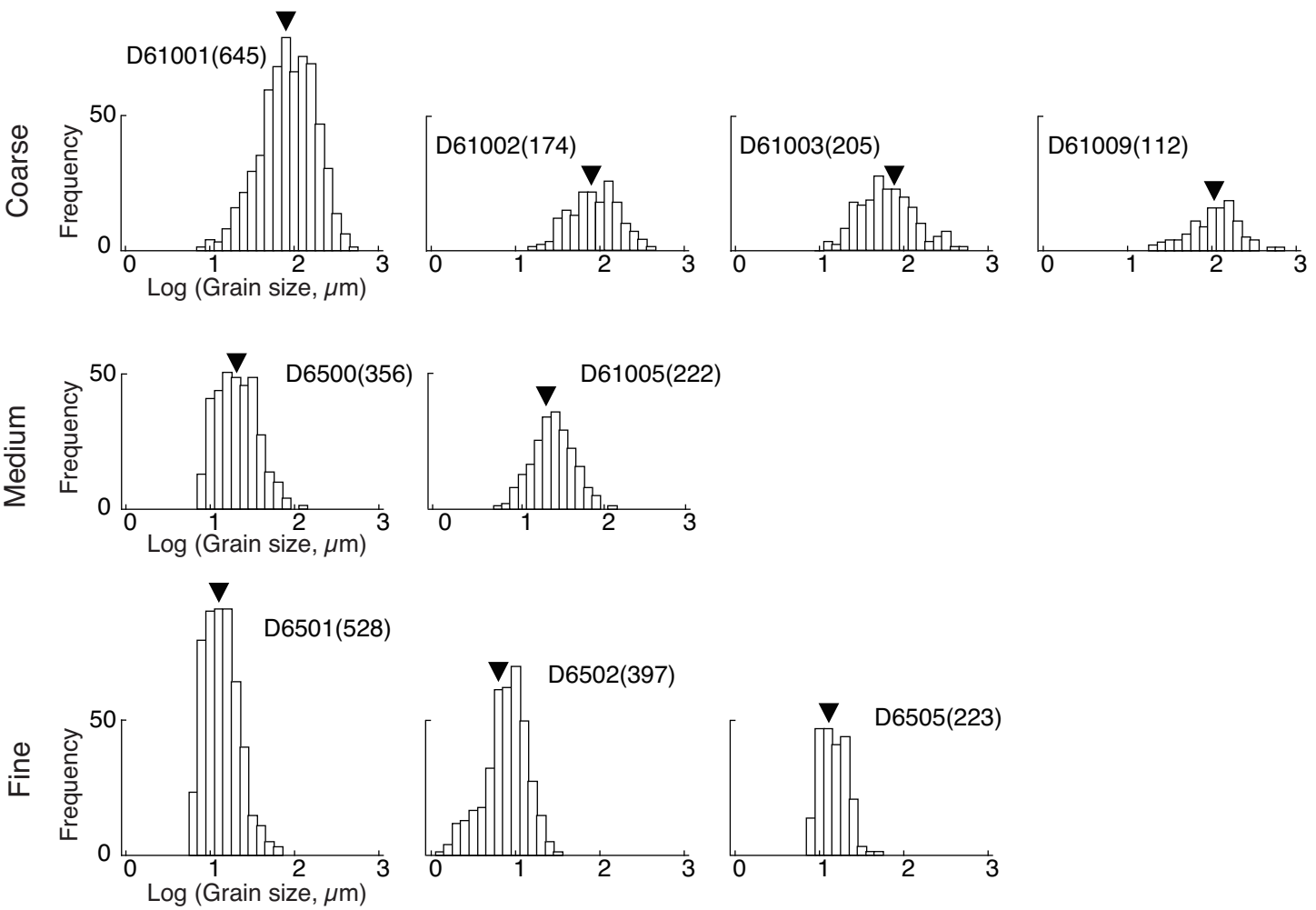Figure 2

Figure 2. Harigane et al.

Figure3

Figure 3

Figure 3. Harigane et al.

Figure 4
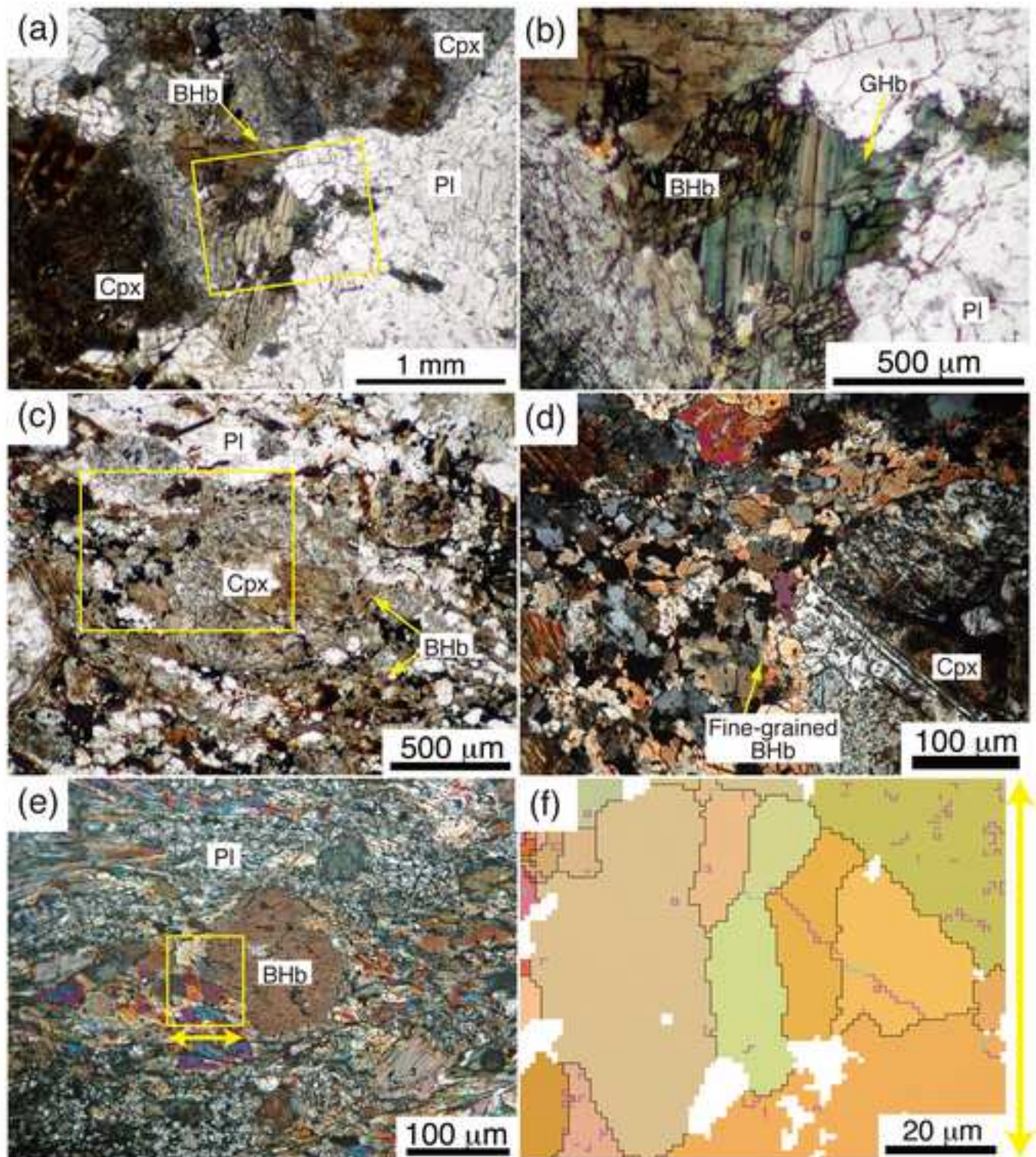
Figure 4. Harigane et al.

Figure5
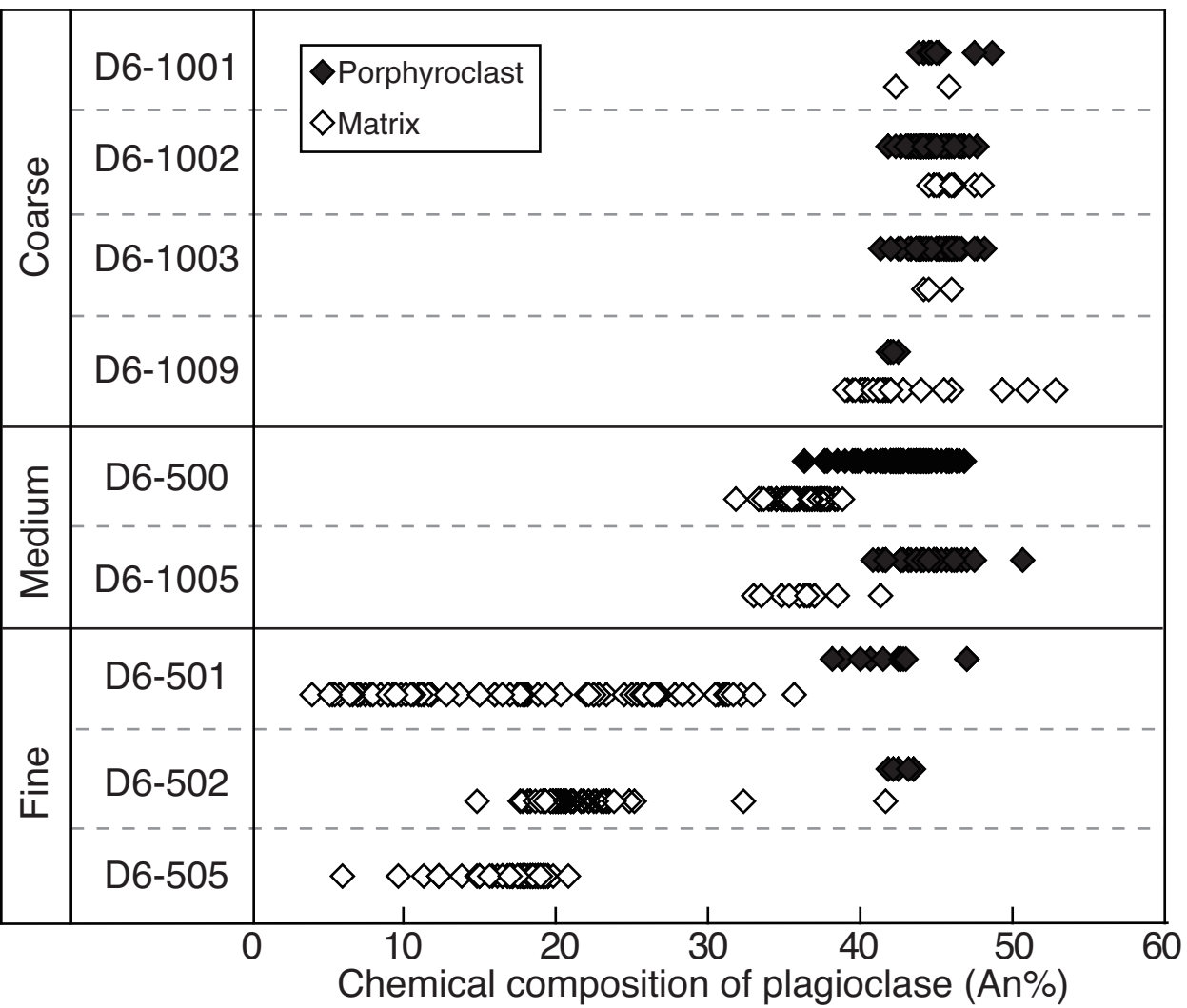
Figure 5

Figure 5. Harigane et al.

Figure6

Figure 6

(a)

(b)
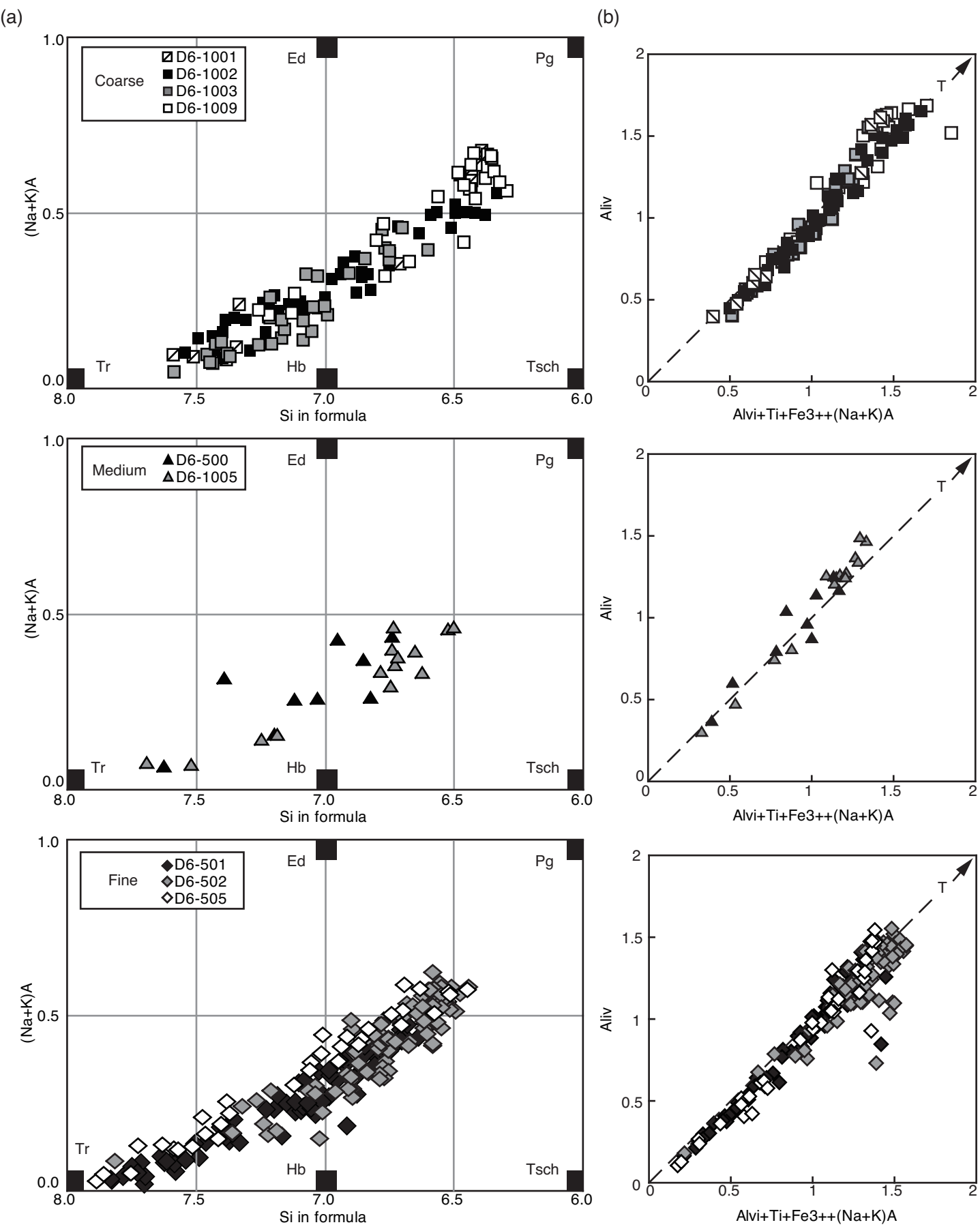
Figure 6. Harigane et al.

Figure 7

(a)   Plagioclase   (b)   Hornblende

[100]   (010)   (001)   (100)   (010)   [001]
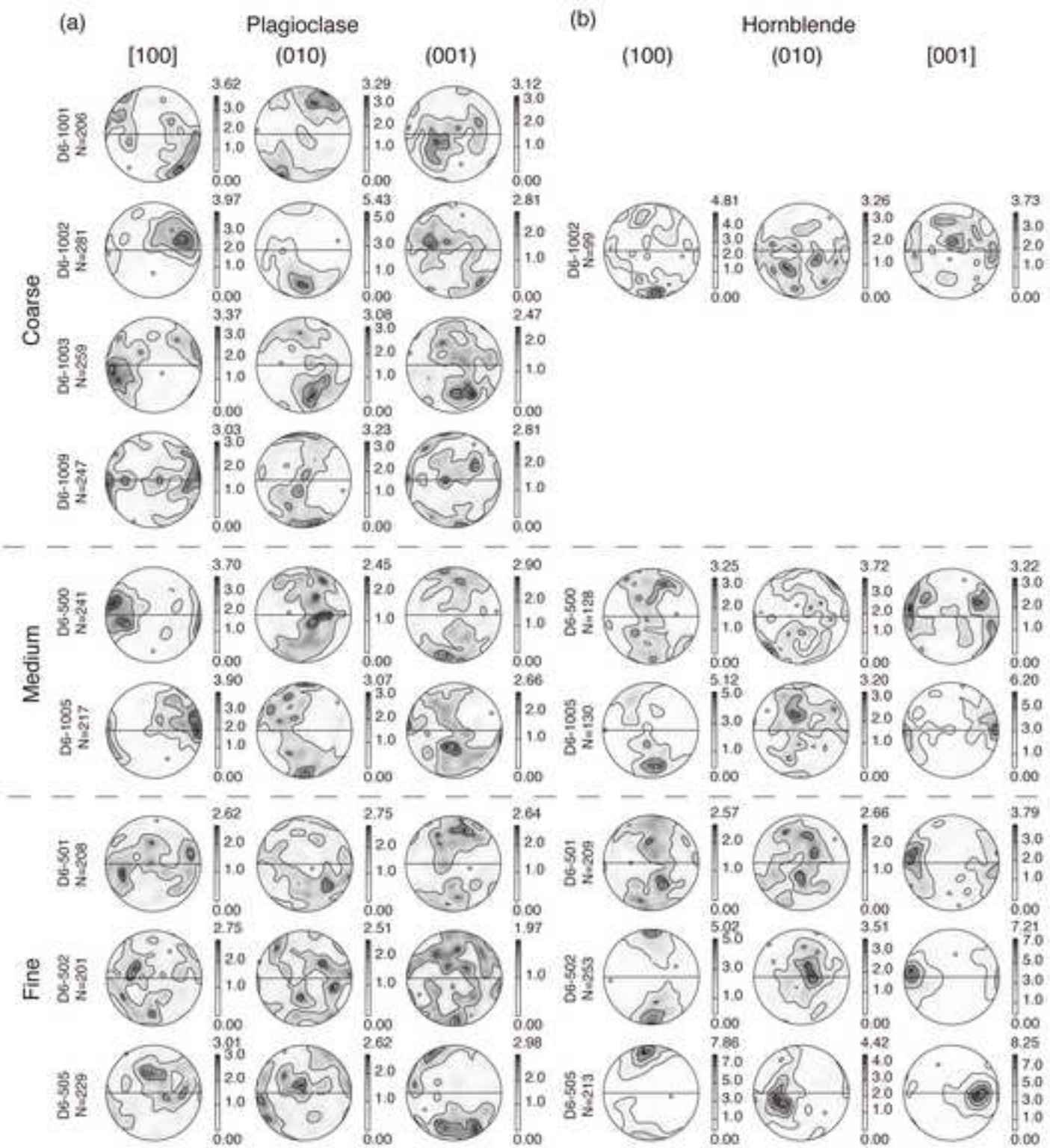
Figure 7. Harigane et al.

Figure8

Figure 8

[100] (010) (001)

Coarse
D6-1002

■ porphyroclasts (N=23)
□ matrix grains (N=127)

Medium
D6-1005

■ porphyroclasts (N=31)
□ matrix grains (N=177)

Fine
D6-502

■ mixed layer (N=229)
□ mono layer (N=161)
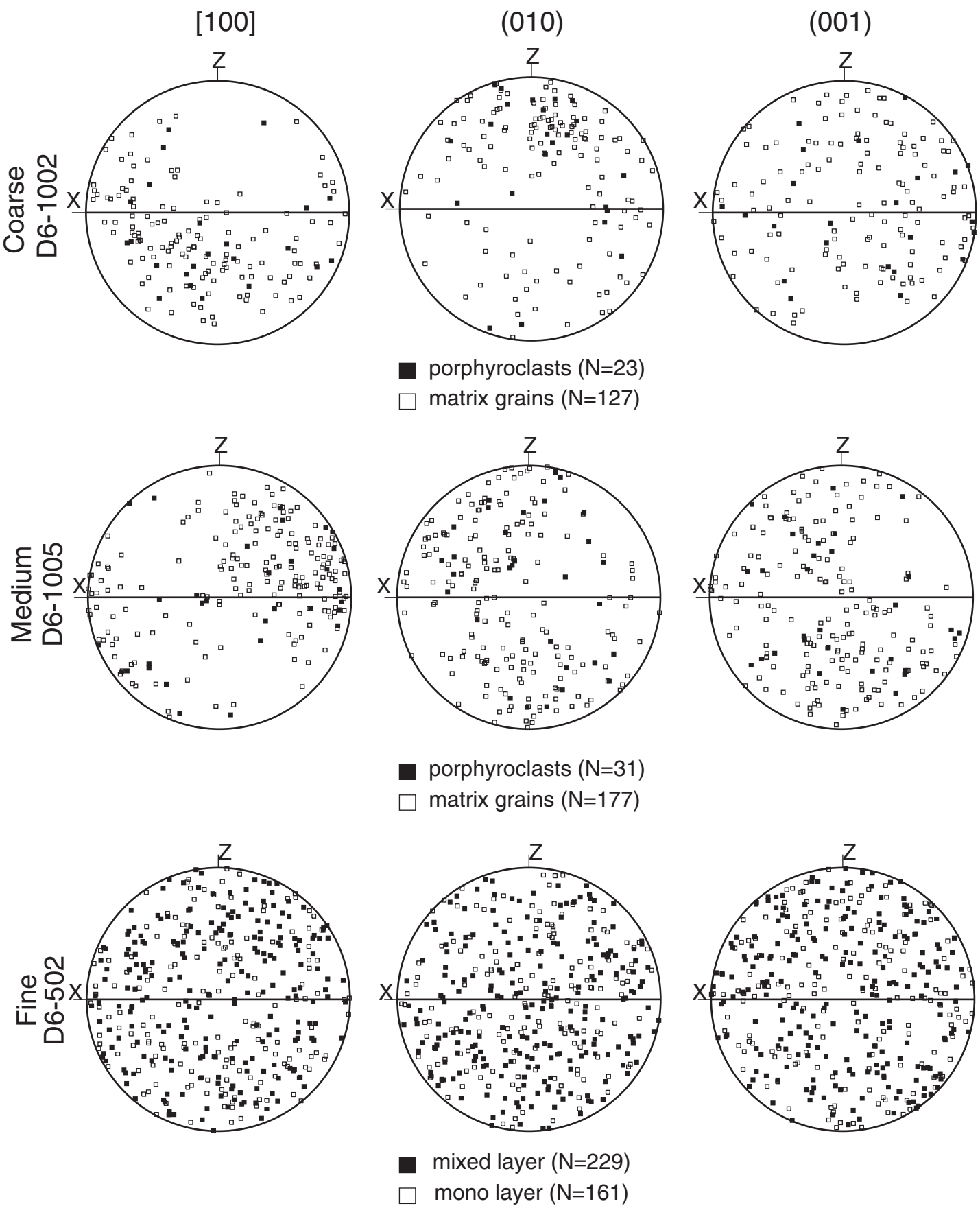
Figure 8. Harigane et al.

Figure9

Figure 9

(100)　　　　　　　　　　(010)　　　　　　　　　　[001]

Fine
D6-502

■ mixed layer (N=140)
□ mono layer (N=160)

Figure 9. Harigane et al.

Figure10

Figure 10

(a) Coarse (D6-1002)

(b) Medium (D6-1005)

(c) Fine (D6-502)

500   600   700   800   900

Temperature (^{o}C)

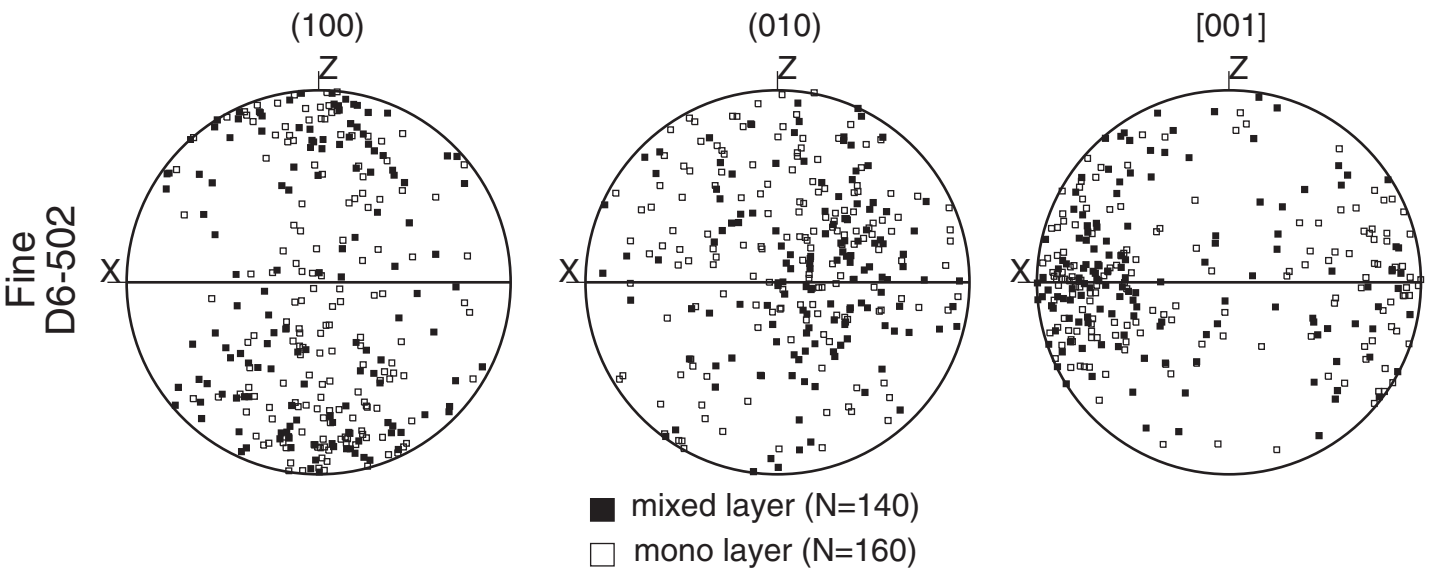**Figure 10. Harigane et al.**
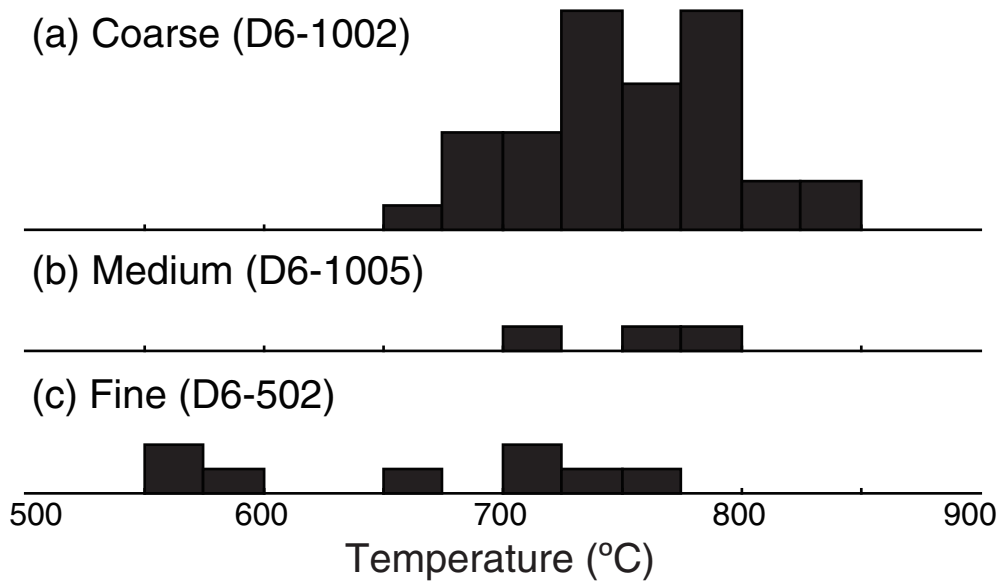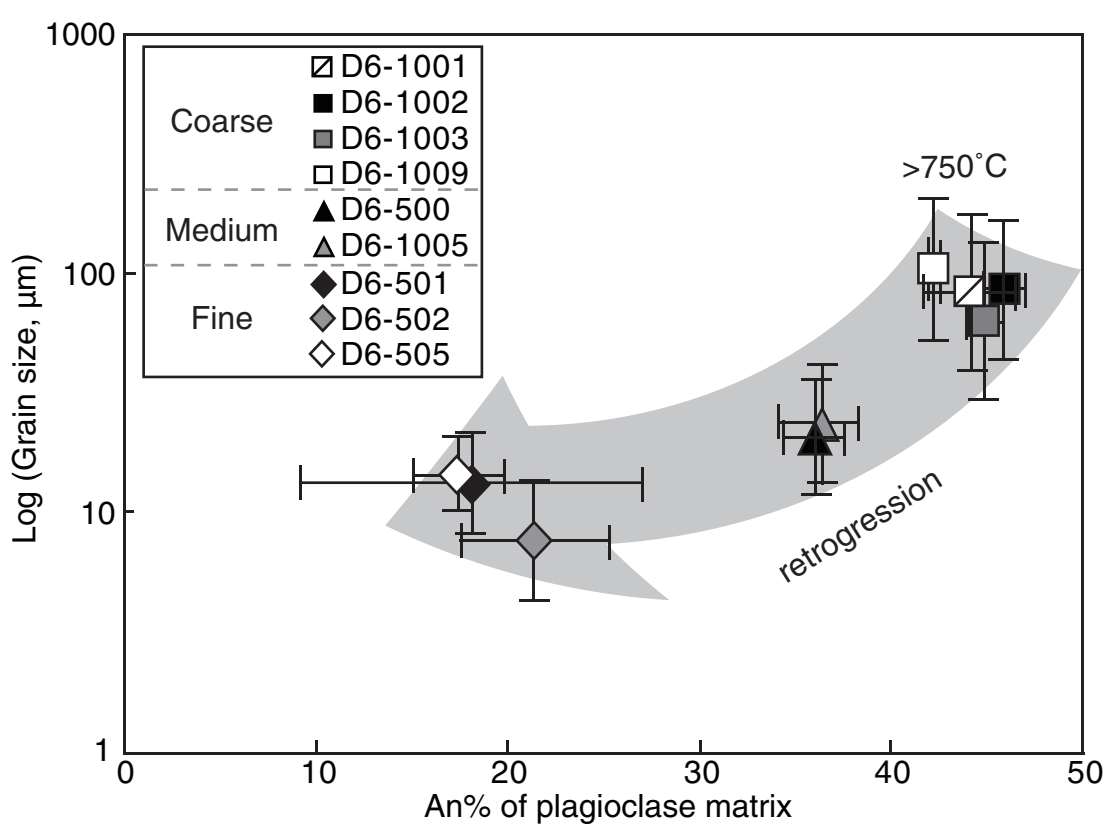
Figure11

Figure 11
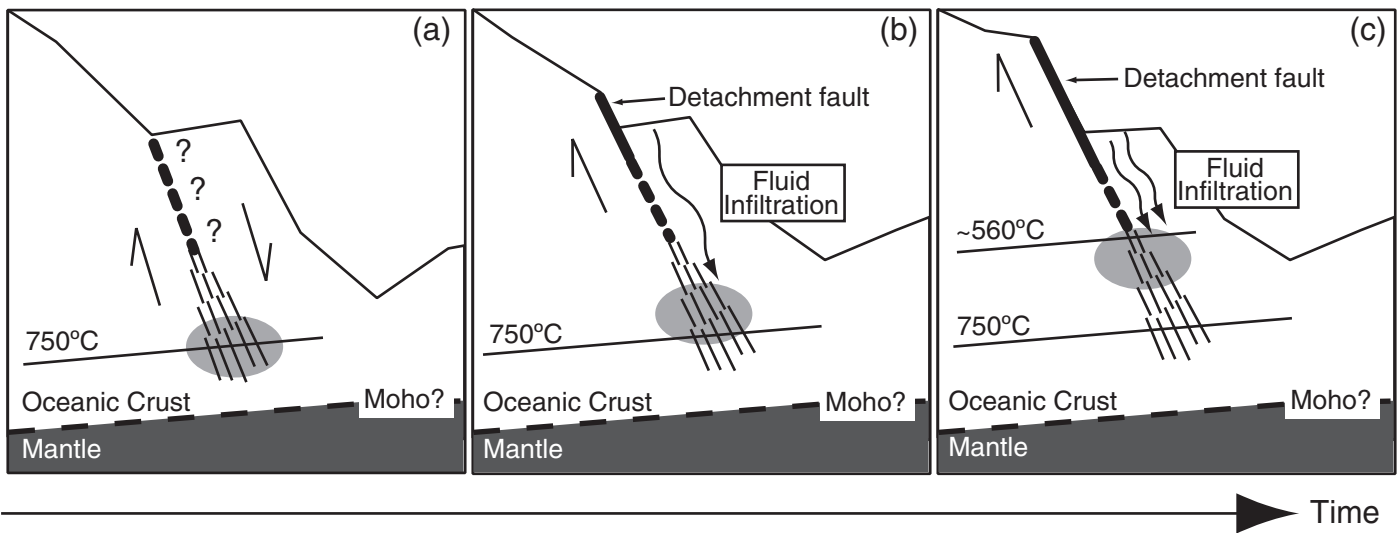

Figure 11. Harigane et al.

Figure12

Figure 12

Figure 12. Harigane et al.

Table1. The features of analyzed gabbroic rocks

Sample number	D6-1001	D6-1002	D6-1003	D6-1009	D6-500	D6-1005	D6-501	D6-502	D6-505
Microstructure	mylonitic gabbro coarse size matrix				mylonitic gabbro medium size matrix		ultramylonite fine size matrix		
Mineral assemblage	Pl, Cpx, Amp(including brown Hb and green Hb), Ilm, Mt, Ap				Pl, Cpx, Amp(including brown Hb and green Hb), Ilm, Mt, Ap, Chl		Pl, Amp(including brown Hb and green Hb), Ilm, Mt, Ap, Chl		
Mineral mode (%)	-	Pl: 55.2 Cpx: 13.8 Amp: 18.1 Ilm & Mt: 9.35 Others: 3.6	Pl: 51 Cpx: 25.25 Amp: 7.2 Ilm & Mt: 2.5 Others: 14.05	Pl: 36.9 Cpx: 23.05 Amp: 5.05 Ilm & Mt: 18.9 Others: 16.1	Pl: 48.25 Cpx: 12 Amp: 21.85 Ilm & Mt: 9.25 Others: 8.65	Pl: 42.75 Cpx: 11.2 Amp: 17.65 Ilm & Mt: 15.3 Others: 13.1	Pl: 25.6 Amp: 55.05 Ilm & Mt: 10.2 Others: 9.15	Pl: 23.1 Amp: 72.194 Ilm & Mt: 0.805 Others: 3.907	Pl: 63.82 Amp: 30.32 Ilm & Mt: 1.86 Others: 4
Pl matrix Average grain-size (µm)	107.3	105.1	83.9	129.8	24.0	27.8	15.3	8.9	15.6
Pl porphyroclast anorthite contents	45.3	44.6	45.0	42.4	42.7	44.2	42.1	42.6	-
Pl matrix anorthite contents	44.1	45.9	44.9	42.2	35.9	36.3	18.1	21.4	17.4

Pl: plagioclase, Cpx: clinopyroxe, Amp: amphibole, Ilm: ilmenite, Mt: magnetite, Ap: apatite, Chl: chlorite.
Others in mineral mode includes chlorite, apatite and crack.

Table 2. Microprobe analyses of plagicoclase. Fe* is calculated by all Fe^{2+}.
P- and M- are porphyroclast and matrix grain, respectivity.

Thin section	D6-1002		D6-1005		D6-502	
Analysis No.	P-6	M-34	P-917	M-859	P-418	M-556
SiO_2	58.31	57.13	57.30	60.33	57.38	63.79
TiO_2	0.12	0.05	0.23	0.08	0.10	0.02
Al_2O_3	26.65	26.56	26.48	25.01	26.89	22.85
FeO	0.22	0.20	0.63	0.27	0.10	0.30
MnO	0.00	0.03	0.00	0.00	0.01	0.00
MgO	0.00	0.00	0.00	0.00	0.01	0.03
CaO	9.33	8.85	9.00	7.46	8.85	4.41
Na_2O	6.24	6.33	6.17	7.22	6.43	8.80
K_2O	0.07	0.03	0.05	0.13	0.04	0.01
total	100.93	99.17	99.85	100.49	99.80	100.22
Cations / O	8	8	8	8	8	8
Si	2.589	2.580	2.576	2.677	2.575	2.811
Ti	0.004	0.002	0.008	0.003	0.003	0.001
Al	1.394	1.414	1.403	1.308	1.422	1.187
Fe*	0.008	0.008	0.024	0.010	0.004	0.011
Mn	0.000	0.001	0.000	0.000	0.000	0.000
Mg	0.000	0.000	0.000	0.000	0.000	0.002
Ca	0.444	0.428	0.433	0.354	0.425	0.208
Na	0.538	0.554	0.538	0.621	0.559	0.752
K	0.004	0.001	0.003	0.007	0.002	0.001
total	4.981	4.989	4.985	4.981	4.992	4.972
An%	45.04	43.52	44.49	36.06	43.10	21.68

Table 3. Microprobe analyses of clinopyroxene.
Fe* is calculated by all Fe^{2+}.

Thin section	D6-1002	D6-1002	D6-1005	D6-1005
Analysis No.	CPX-26	CPX-33	CPX-832	CPX-882
SiO_2	50.50	51.19	51.50	52.21
TiO_2	0.86	0.88	0.43	0.17
Al_2O_3	2.54	2.62	1.20	1.01
FeO	11.14	12.83	11.60	12.16
MnO	0.30	0.39	0.30	0.29
MgO	12.59	13.71	12.41	12.89
CaO	22.16	17.88	21.81	20.45
Na_2O	0.58	0.65	0.32	0.28
K_2O	0.01	0.00	0.00	0.01
total	100.68	100.14	99.57	99.46
Cations / O	6	6	6	6
Si	1.900	1.924	1.957	1.979
Ti	0.024	0.025	0.012	0.005
Al	0.113	0.116	0.054	0.045
Fe*	0.351	0.403	0.369	0.385
Mn	0.010	0.013	0.010	0.009
Mg	0.706	0.768	0.703	0.729
Ca	0.893	0.720	0.888	0.830
Na	0.042	0.047	0.023	0.021
K	0.000	0.000	0.000	0.001
total	4.040	4.016	4.016	4.004
Mg/Mg+Fe	0.668	0.656	0.656	0.654
Wo	45.81	38.06	45.30	42.71
En	36.22	40.61	35.89	37.47
Fs	17.98	21.33	18.81	19.82

Table 4. Representive compoitions of amphiboles in gabbroic rocks.
Estimate of Fe^{3+} follow Holland and Blundy (1994).

Thin section	D6-1002		D6-1005		D6-502	
Analysis No.	Amp-15 Act	Amp-67 Pg	Amp-844 Act	Amp-904 Mg-Hb	Amp-313 Act	Amp-538 Pg
SiO_2	51.40	41.36	51.23	43.18	54.50	43.35
TiO_2	0.22	0.90	0.31	2.73	0.17	1.83
Al_2O_3	2.71	9.49	3.26	9.40	1.16	9.53
FeO	15.87	24.59	18.75	18.20	14.70	17.06
MnO	0.28	0.26	0.25	0.12	0.26	0.19
MgO	13.84	6.37	13.78	10.22	15.53	11.71
CaO	11.89	11.15	9.19	11.20	11.75	10.20
Na_2O	0.59	1.83	0.51	1.83	0.48	2.38
K_2O	0.03	0.20	0.06	0.20	0.02	0.11
total	96.82	96.15	97.34	97.08	98.56	96.36
Cations / O	23	23	23	23	23	23
Si	7.551	6.462	7.521	6.504	7.815	6.496
Al^{iv}	0.449	1.538	0.479	1.496	0.185	1.504
Al^{vi}	0.019	0.209	0.085	0.173	0.011	0.178
Ti	0.024	0.106	0.035	0.309	0.018	0.206
Fe^{3+}	0.348	0.698	0.344	0.349	0.105	0.609
MgC	3.031	1.485	3.015	2.294	3.319	2.614
Fe^{2+}	1.601	2.515	1.957	1.942	1.657	1.528
Mn	0.034	0.034	0.032	0.015	0.032	0.024
Ca	1.871	1.867	1.445	1.807	1.805	1.637
Na	0.169	0.554	0.144	0.535	0.133	0.692
K	0.006	0.039	0.012	0.038	0.004	0.021
total	15.10	15.51	15.07	15.46	15.09	15.51